

# Studies of noctilucent clouds from the stratosphere during the 2024 TRANSAT balloon flight

Peter Dalin<sup>1</sup>, Hidehiko Suzuki<sup>2</sup>, Nikolay Pertsev<sup>3</sup>, Vladimir Perminov<sup>3</sup>, Linda Megner<sup>4</sup>, Johan Kero<sup>1</sup>, Peter Voelger<sup>1</sup>, Jonas Hedin<sup>4</sup>, Gerd Baumgarten<sup>5</sup>, Anne Réchou<sup>6</sup>, Denis Efremov<sup>7</sup>

<sup>1</sup> Swedish Institute of Space Physics, Kiruna, Sweden

<sup>2</sup> School of Science and Technology, Meiji University, Kawasaki, Japan

<sup>3</sup> A.M. Obukhov Institute of Atmospheric Physics RAS, Moscow Russia

<sup>4</sup> Department of Meteorology (MISU), Stockholm University, Stockholm, Sweden

<sup>5</sup> Leibniz Institute of Atmospheric Physics, Rostock University, Kühlungsborn, Germany

<sup>6</sup> Lacy Laboratory of Atmosphere and Cyclones, Université de La Réunion, Réunion, France

<sup>7</sup> Aerospace Laboratory “Stratonautica”, Moscow, Russia

*Correspondence to:* Peter Dalin (pdalin@irf.se)

**Abstract.** A transatlantic scientific balloon flight (TRANSAT) was conducted between 22 and 26 June 2024. The TRANSAT balloon, operated by the French Space Agency (CNES), floated in the stratosphere at approximately 40 km altitude between Esrangle (Sweden) and Baffin Island (Canada) for about 3.8 days. The scientific payload comprised nine instruments, including an optical imager for noctilucent cloud (NLC) studies from the Swedish Institute of Space Physics. The NLC imager consisted of three identical visible-range optical cameras, one of which operated successfully throughout the entire flight, capturing thousands of NLC images. The TRANSAT balloon campaign was supported by ground-based lidar measurements and spaceborne observations from the Swedish MATS satellite. Here, we describe the technical characteristics of the balloon experiment and present early results. Nearly continuous observations of NLC were obtained during the entire flight. A localized warm region in the mesopause was identified as the cause of temporary NLC disappearance, while complex NLC structures exhibiting different motions were found to probably result from horizontal wind rotation with altitude within the mesopause region.

## 1 Introduction

Noctilucent clouds (NLC) are the highest clouds in the Earth’s atmosphere, forming in the summer mesopause region between 80 and 90 km altitude at middle and polar latitudes in both hemispheres. They consist of water-ice particles with radii of 30–100 nm that scatter sunlight, making the clouds visible against the twilight sky. NLCs are typically observed from May to September in the Northern Hemisphere and from November to February in the Southern Hemisphere (Gadsden and Schröder, 1989; Liu et al., 2016). When observed from space, these clouds are traditionally called Polar Mesospheric Clouds (PMC) (Thomas, 1984).

NLC and PMC are systematically studied using ground-based optical cameras, spectrographs, lidars as well as dedicated spaceborne instruments (e.g., Karlsson and Gumbel, 2005; Dalin et al., 2008; Bailey et al., 2009;

39 Fiedler et al., 2011; DeLand and Thomas, 2015; Tsuda et al., 2022; Wallis et al., 2025). In addition, irregular  
40 campaign-based NLC observations are carried out using sounding rockets and aircraft (Zadorozhny et al., 1993;  
41 Gumbel and Witt, 2001; Reimuller et al., 2011; Suzuki et al., 2022; Pertsev et al., 2024). Each observational  
42 technique has specific advantages and limitations. In particular, ground-based imagers offer high horizontal (~20  
43 m) and temporal (~1 s) resolution (Dalin et al., 2010; Baumgarten and Fritts, 2014), and lidars provide high  
44 vertical resolution (50–150 m; Baumgarten et al., 2009), but both are restricted by tropospheric weather and  
45 limited geographic coverage. Conversely, satellite observations deliver global PMC coverage but suffer from  
46 low spatial (~1 km) and temporal (minutes to hours) resolution. Moreover, sun-synchronous satellites introduce  
47 large spatial gaps (hundreds of km) between adjacent orbits at mid- and subpolar latitudes (45–60°N) due to a  
48 spacecraft orbiting the Earth. Consequently, no single existing technique can fully resolve the microphysical and  
49 dynamical processes governing NLC/PMC.

50 Balloon-borne observations from stratospheric altitudes (25–40 km) have a potential for comprehensive  
51 studies of NLC on a regular basis. Such observations provide several advantages: independence from  
52 tropospheric weather, uninterrupted 24 h coverage, and proximity to the NLC layer (80–85 km), yielding the  
53 highest achievable spatial resolution. From this vantage point, both large-scale (up to 2500 km, limited by  
54 Earth’s curvature) and small-scale (down to meters) NLC features can be observed. Furthermore, balloon-borne  
55 observations at 30–40 km altitude occur above the ozone-rich layer (20–25 km), thereby avoiding light  
56 absorption in the Chappuis band (400–650 nm).

57 To date, four balloon-borne experiments have been dedicated to NLC observations from the stratosphere  
58 (Miller et al., 2015; Dalin et al., 2019, 2020, 2022; Fritts et al., 2019). These missions have provided unique  
59 datasets for studying both large- and small-scale wave dynamics and turbulence within NLC layers. The  
60 motivation for the NLC experiment on board the 2024 TRANSAT flight are as follows:

- 61 1. Investigation of temporal-spatial variability of NLC at large- and small-scales in the subpolar and polar  
62 mesopause for several days.
- 63 2. Quantification of atmospheric gravity waves at large- and small-scales and turbulent processes, with  
64 modeling of propagation pathways and search for wave sources in the underlying atmosphere.
- 65 3. Gaining experience in conducting experiments in the stratosphere for several days.

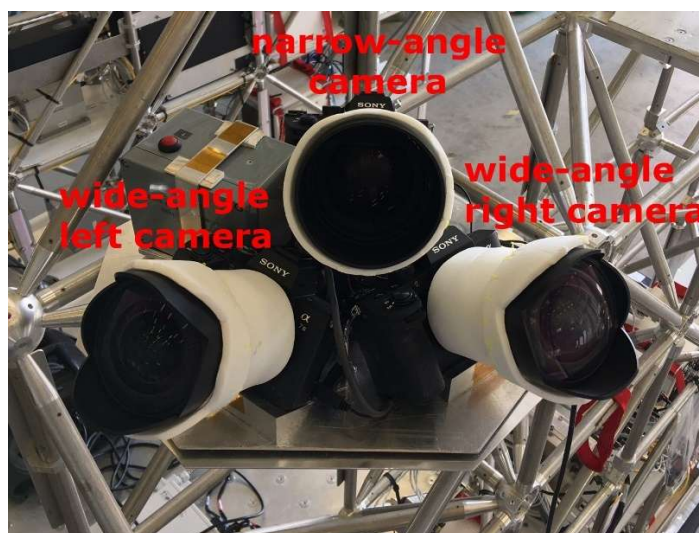
66 In this study, we present results from a new long-duration balloon experiment aimed at investigating NLC in  
67 the polar mesopause. We describe the observation technique and instrumentation as well as early scientific  
68 findings. The stratospheric NLC observations were complemented by ground-based lidars and, for the first time,  
69 by spaceborne measurements from the Swedish MATS satellite. Additionally, temperature and water vapor data  
70 from the Aura/MLS satellite were used to characterize the mesopause environment during the TRANSAT flight,  
71 and JAWARA model data were employed to simulate the thermodynamic and wind conditions in support of the  
72 NLC observations.

## 73 **2 Technique and method**

### 74 **2.1 Technical characteristics of the imager**

75 The Stratospheric Observations of Noctilucent Clouds (SONC) experiment is a balloon-borne scientific  
76 mission designed to investigate NLC dynamics across a broad range of spatial scales—from large-scale  
77 structures (30–2500 km) to fine-scale features (5 m–30 km)—as well as the microphysical properties of NLC ice  
78 particles.

79 To achieve these objectives, three high-resolution, high-sensitivity Sony  $\alpha 7$  Mark III cameras were used.  
 80 Each camera has a full-frame 35 mm, 24-megapixel sensor ( $6000 \times 4000$  pixels). Two cameras were equipped  
 81 with wide-angle lenses (field of view, FoV,  $=105.4^\circ \times 81.8^\circ$ ), while the third carried a narrow-angle lens  
 82 (FoV $=15.0^\circ \times 10.1^\circ$ ). This configuration, two wide-angle and one narrow-angle camera, provides a horizontal  
 83 coverage of about  $180^\circ$  for studying mesospheric NLC structures up to 2500 km across, while simultaneously  
 84 enabling spatial resolution as fine as about 5 m when viewing the NLC layer at 83 km from a 40 km altitude and  
 85  $35^\circ$  elevation angle. Note that such simultaneous access to both large and small scales is currently unattainable  
 86 from either ground-based or satellite platforms. The three cameras formed the SONC imager, illustrated in Fig.  
 87 1. Each camera stored data on two 1 TB SD cards. Given the expected 4–5 day duration of the transatlantic flight  
 88 and the storage limits, an image acquisition cadence of 50 s was chosen. This temporal resolution enables  
 89 tracking the evolution of small-scale wave activity within the NLC layer as well as monitoring large-scale cloud  
 90 dynamics. The optical axes of the two wide-angle cameras were inclined at  $36^\circ$  to the horizontal plane in order to  
 91 minimize light contamination from bright tropospheric scattering and from above coming from a big white  
 92 balloon envelope ( $\sim 70$  m in diameter). The narrow-angle camera was tilted at  $35^\circ$  to the horizontal plane to  
 93 resolve fine-scale structures of NLC.



94  
 95 **Figure 1: The SONC imager consists of three Sony  $\alpha 7$  Mark III cameras and the electronic control unit**  
 96 **(gray box with red button). Two cameras are equipped with wide-angle lenses, and one with a narrow-**  
 97 **angle lens positioned between them. The instrument was used to observe noctilucent clouds during the**  
 98 **TRANSAT transatlantic balloon flight (22–26 June 2024).**

99  
 100 Sony  $\alpha 7$  Mark III camera has a standard Micro USB terminal for power supplying, battery charging and USB  
 101 communications, into which an external trigger can be connected to activate the shutter button. For this purpose,  
 102 we have developed an external trigger (gray box shown in Fig. 1) that simultaneously transmits the trigger signal  
 103 to all three NLC cameras at a certain cadence time (50 s in this experiment). Thus, automatic shooting is carried  
 104 out by the three cameras throughout the balloon flight. In addition, this external device distributes power to all  
 105 three cameras from an external power supply (a chemical battery on the gondola).

106 Automatic exposure bracketing was applied, capturing 5 images sequentially with exposure times varying  
 107 between  $1/1600$  s and 1.6 s. This approach accommodated a wide dynamic range of NLC brightness under  
 108 variable atmospheric background illumination conditions. One wide-angle camera (left in Fig. 1) operated

109 flawlessly throughout the 3.8-day flight, producing a total of about 40,000 images. The other wide-angle and the  
110 narrow-angle cameras functioned for the first 13 h and 12 h, respectively, before ceasing operation for unknown  
111 reasons. The imager survived the gondola landing on the ice of Baffin Island without damage. Post-flight tests of  
112 all the cameras and electronics confirmed full functionality of the SONC imager and no performance  
113 degradation. It should be noted that all three cameras had already been in the stratosphere for about 13 hours at  
114 low temperatures of  $-30^{\circ}\text{C}$  and were functioning normally (Dalin et al., 2022). Taking into account the previous  
115 positive balloon-borne experiment, it was decided to use all three cameras for the long-duration TRANSAT  
116 flight in the stratosphere. Also note that SONY  $\alpha 7$  Mark III cameras are commercial cameras that are not  
117 designed for a flight in the stratosphere in 24/7 sunlight, at low temperatures and low thermal conductivity due to  
118 rarefied air. The electronics inside the two cameras could freeze or overheat. This is the most likely reason for  
119 the failure of these two cameras after 12 h of the flight.

120

## 121 **2.2 Technical characteristics of the TRANSAT balloon flight**

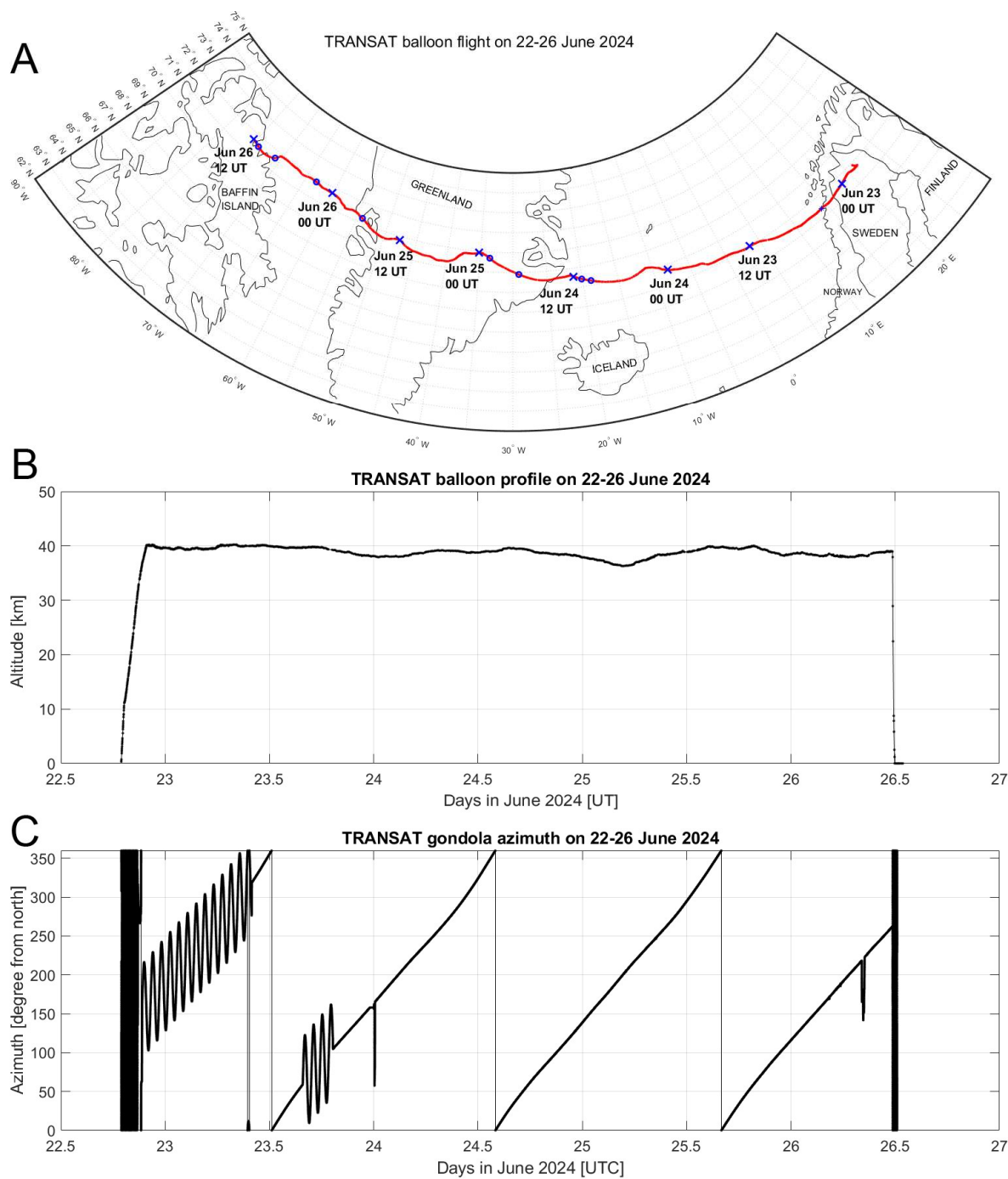
122 The TRANSAT mission is a long-duration stratospheric balloon flight organized and operated by the French  
123 Space Agency (CNES) for multidisciplinary atmospheric and cosmic research. The gondola, named Carmen, had  
124 a total mass of about 900 kg and carried nine scientific instruments. Two of these were from Sweden: the SONC  
125 imager and an infrasound instrument dedicated to studies of infrasound atmospheric waves and their sources.  
126 The infrasound experiment and its scientific results will be described in a separate paper.

127 The Carmen gondola utilized a three-axis motorized gimbal stabilized platform, providing an elevation-angle  
128 stability of  $0.15^{\circ}$ , an absolute azimuth pointing accuracy of  $1^{\circ}$  and a stability of  $\pm 10$  arcmin around it. Because  
129 stratospheric balloons rotate continuously, such stabilization was critical to avoid image smearing and to  
130 maintain consistent NLC monitoring at fine and large scales.

131 As the transatlantic flight took place under solstice conditions with continuous solar illumination, scientific  
132 instruments were mounted behind a solar shield to prevent overheating and stray-light interference. To ensure  
133 continuous shading, the gondola was slowly rotated to keep the solar shield facing the Sun throughout the flight.  
134 Due to different scientific experiments onboard requiring different pointing directions, sometimes the anti-sun  
135 direction was not observed, but the oscillations around the leading azimuth of the gondola remained under  
136 control (see Fig. 1c). When the Sun illuminated the camera lens or strong solar reflections were present, such  
137 images were removed from the image analysis as overexposed. The number of the overexposed removed image  
138 accounted for about 2% of the total number of images analyzed.

139 The TRANSAT balloon was launched from Esrangle, northern Sweden ( $67.89^{\circ}\text{N}$ ,  $21.08^{\circ}\text{E}$ ) at 18:57 UTC  
140 (20:57 LT) on 22 June 2024 and landed on Baffin Island, northern Canada, at 12:14 UTC (08:14 LT) on 26 June  
141 2024. The total flight time was about 90 h (3.8 days), with an average horizontal speed of about  $11\text{ m s}^{-1}$ . The  
142 horizontal trajectory and altitude profiles of the TRANSAT mission are shown in Fig. 2.

143



144  
 145 **Figure 2: (A) Horizontal trajectory (the red line) of the TRANSAT balloon mission between 22 and 26**  
 146 **June 2024. The blue crosses mark the balloon’s position every 12 h. The blue circles show the balloon’s**  
 147 **positions when no NLC were observed, see Section 4.1. (B) Altitude profile of the TRANSAT flight. (C)**  
 148 **Azimuth of the optical axis of the left camera of the SONC imager due to the TRANSAT gondola rotation**  
 149 **in the anti-sun direction for most of the flight.**

150

### 151 2.3 Image processing

152 Prior to launch, all three Sony cameras underwent geometrical calibration on the ground using night-sky  
 153 images containing reference stars. A second-order polynomial camera model was fitted by comparing theoretical  
 154 and measured horizontal coordinates for over 200 identified reference stars. Six free coefficients describing focal

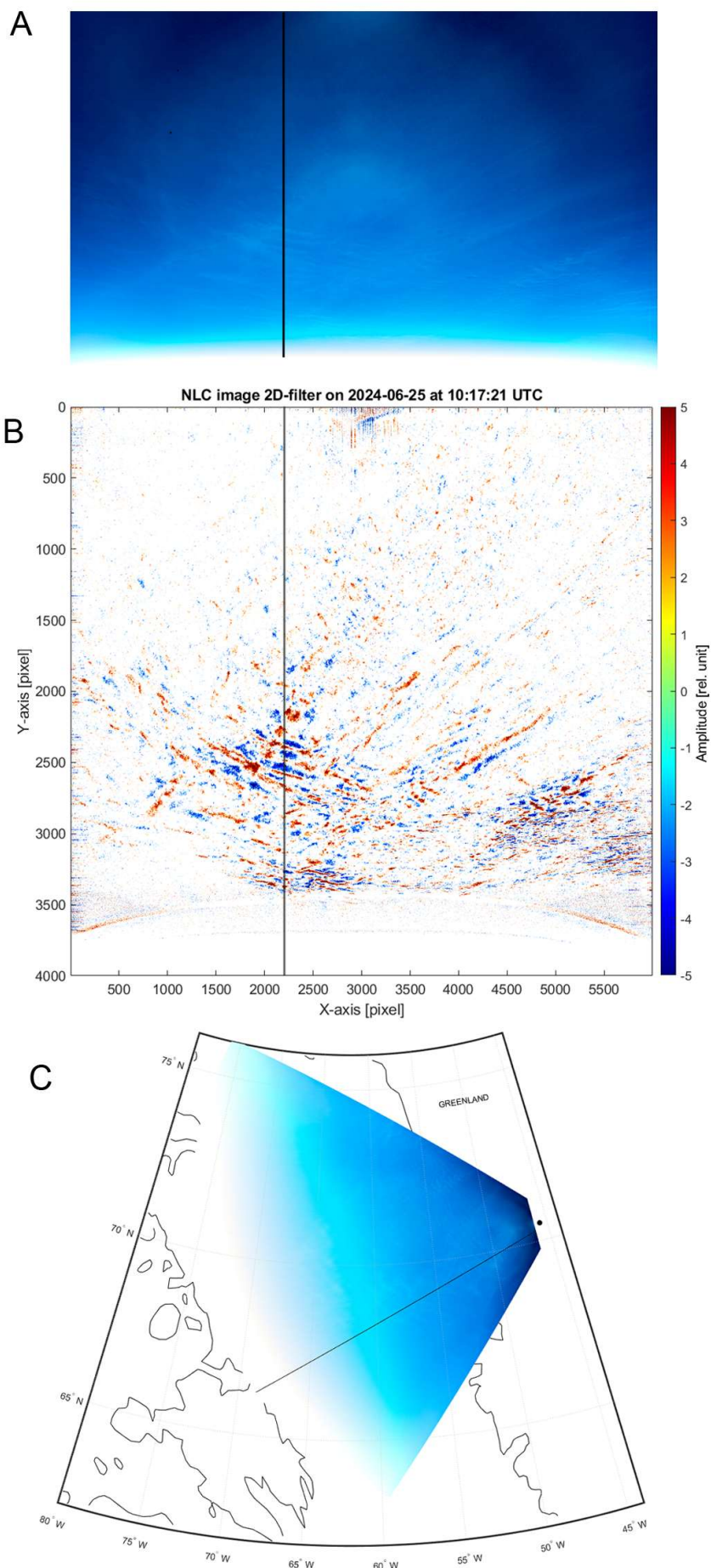
155 length, image orientation, and optical distortion were determined. These coefficients were used to compute  
156 relative horizontal coordinates (elevation and azimuth angles relative to the center of the image) for every pixel  
157 of each camera.

158 Given the known position and orientation of the SONC imager within the gondola reference frame, provided  
159 by CNES, the absolute horizontal coordinates of all pixels were computed. Subsequently, a georeferencing  
160 procedure projected each pixel onto the Earth's surface, assuming a mean NLC altitude of 83 km. Details of the  
161 calibration, georeferencing, and error analysis are available in Dalin et al. (2015).

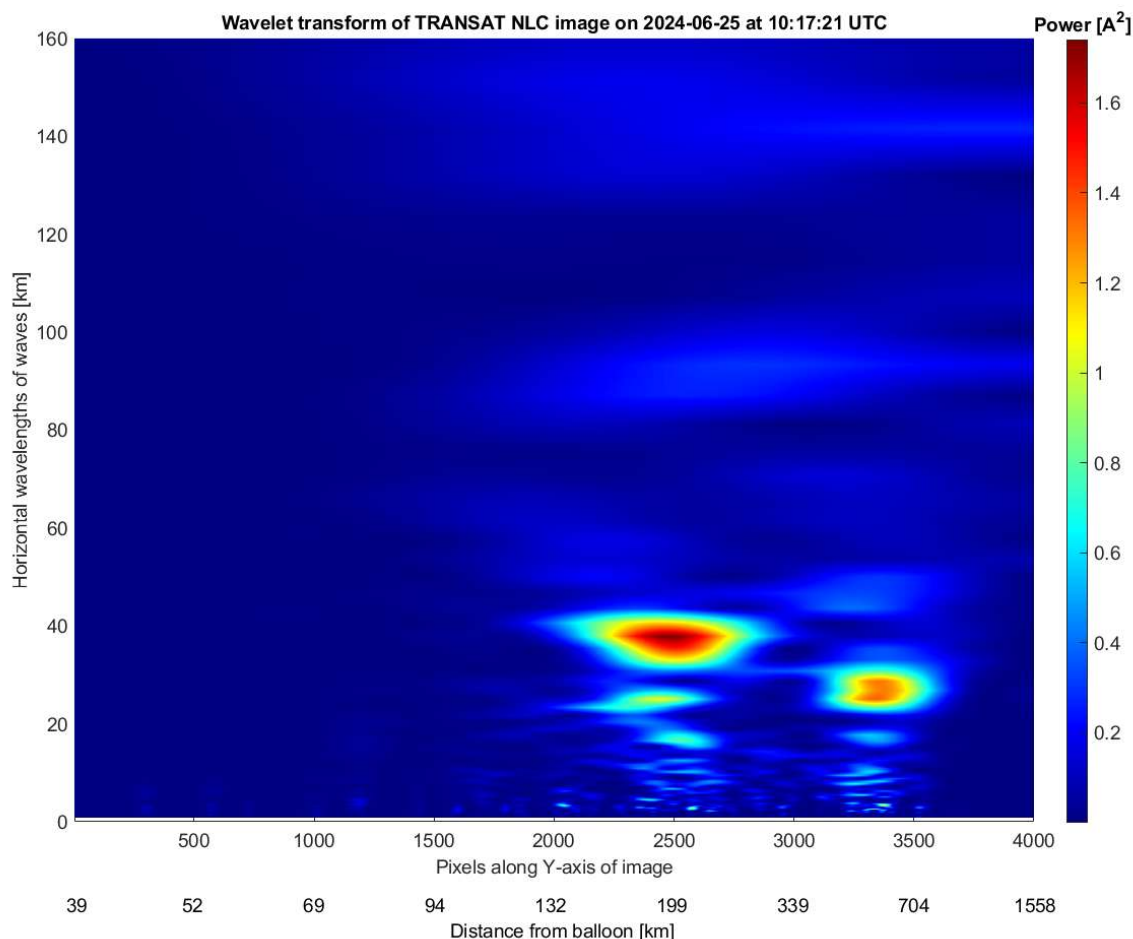
162 NLC identification was performed using both manual and automatic approaches. In the manual procedure,  
163 about 6200 images, suitable for scientific analysis, from the left camera (Fig. 1) were carefully examined to mark  
164 NLC presence or absence. A separate text file was created that indicates the cloud-free times during the  
165 TRANSAT flight. The number of images is 6200 because almost every image in a series of 5 images, taken in  
166 bracketing mode, was analyzed. A video sequence was then assembled to verify temporal continuity. This video,  
167 containing all images with synchronized flight parameters, timestamps and balloon coordinates, is available at  
168 the Harvard Dataverse repository (<https://doi.org/10.7910/DVN/1PHRZU>).

169 Automatic image processing involved several steps: (1) Background subtraction: a second-order polynomial  
170 fit was used to estimate the sky background along each vertical column of pixels, which was then subtracted to  
171 yield a residual brightness of each pixel. (2) Two-dimensional digital filtering: applied to a residual brightness to  
172 extract gravity-wave-like patterns on image (see Fig. 3b). To do this, we use zero-phase digital filtering by  
173 processing the residual brightness in forward and reverse directions along every vertical and horizontal line of  
174 the analyzed image. After filtering the data in the forward direction, the procedure reverses the filtered sequence  
175 and runs it back through the filter that provides a zero-phase distortion. A 4th-order Butterworth bandpass filter  
176 with a lower cutoff frequency of 0.0013 Hz and a higher cutoff frequency of 0.2 Hz is applied in this digital  
177 filtering procedure. (3) Wavelet analysis: a Morse analytic wavelet transform was applied to selected images to  
178 quantify horizontal wavelengths of identified wave patterns. An analyzed image was first projected onto Earth  
179 geographical coordinates (in km) prior to wavelet analysis. An example (Fig. 4) shows dominant horizontal  
180 wavelengths of about 30 and 40 km, which are frequently observed in NLC (Pautet et al., 2011; Demissie et al.,  
181 2014). In the present case, wave analysis was applied to the vertical slice (along the Y-axis) at the constant  
182  $X=2200$  pixels of the filtered image shown in Fig. 3b. This example was chosen at random from 6200 images,  
183 but which demonstrates the NLC modulation due to gravity waves with the naked eye. Therefore, this analysis  
184 technique was applied to this image in order to estimate the horizontal scales of the wave packet in this case.

185 The spatial horizontal resolution of the pixels in the upper part of the projected image (close to the balloon) is  
186 about 21 m, of the pixels in the middle of the image is about 96 m, and of the pixels at the bottom of the  
187 projected image is about 1.2 km. In accordance with the Nyquist–Shannon sampling theorem, these values allow  
188 the study of NLC signals with horizontal scales greater than 42 m, 192 m and 2.4 km, respectively. Thus,  
189 medium- and large-scale gravity waves with horizontal wavelengths greater 50 km, small-scale gravity waves of  
190 10-50 km, smaller-scale localized waves (billows or ripples) of 3-10 km can be analyzed throughout the image.  
191 Also, turbulent structures like vortex rings of 0.5-4 km in diameter can be studied in the upper and middle part of  
192 the image (Dalin et al., 2010; Pautet et al., 2011; Baumgarten and Fritts, 2014; Fritts et al., 2017; Fritts et al.,  
193 2019).



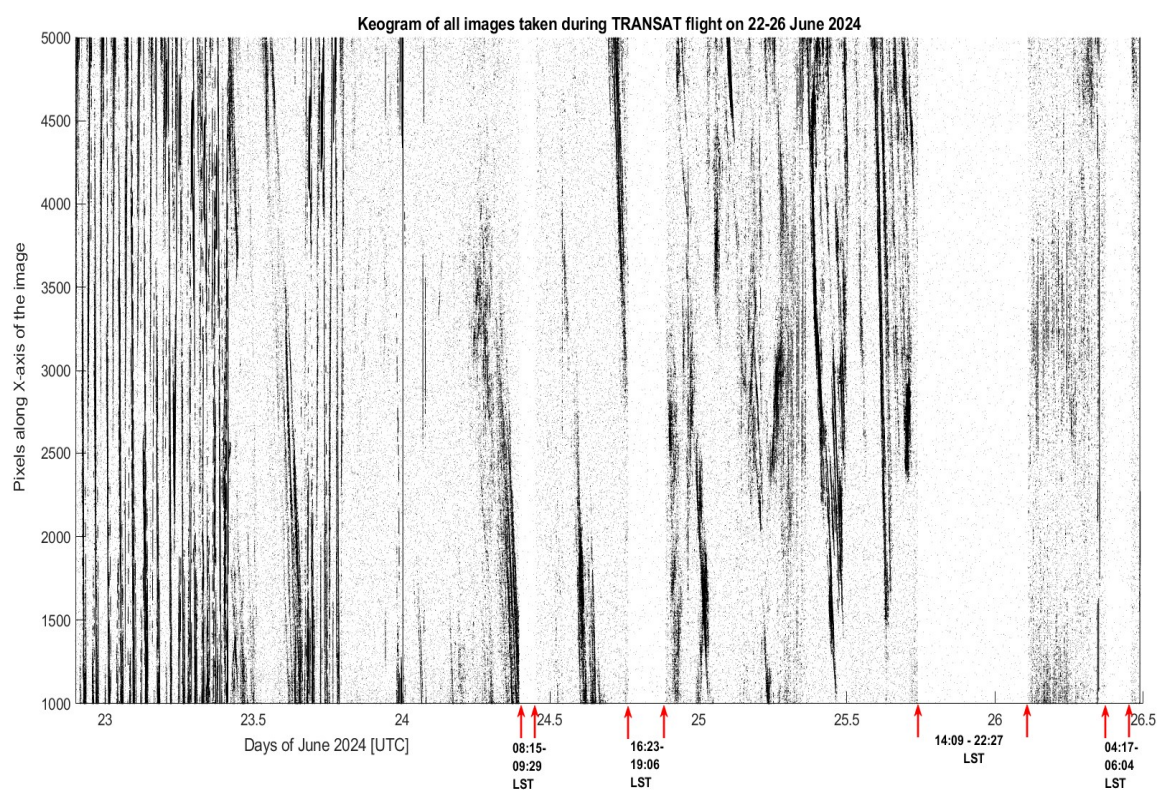
195 **Figure 3: (A) Example of NLC image acquired at 10:17:21 UTC on 25 June 2024 during the TRANSAT**  
 196 **balloon flight. (B) Two-dimensional Fourier-filtered version of (A), highlighting residual brightness**  
 197 **variations associated with NLC bands seen in the middle and the lower part of the image. (C) Projection**  
 198 **of the NLC image shown on panel A onto the Earth's surface. The black dot is the position of the**  
 199 **TRANSAT balloon. The black line shown in panels A, B and C shows the vertical slice at X=2200 pixels**  
 200 **where wavelet analysis was applied (see the text).**  
 201



202 **Figure 4: Example of a wavelet transform for the NLC image obtained at 10:17:21 UTC on 25 June 2024**  
 203 **during the TRANSAT flight. Gravity waves having prevailing horizontal scales of about 30 and 40 km are**  
 204 **clearly seen as the red color code. Two different scales on the X-axis are present: the upper scale is in**  
 205 **pixels along the Y-axis at X=2200 pixels of the image shown in Fig. 3a, the lower scale is the distance from**  
 206 **the TRANSAT balloon in km.**  
 207

208  
 209 4) A keogram representation of a sequence of all analyzed images helps to identify the presence or absence of  
 210 NLC as a function of time. A keogram is a slice of an image along a specific axis, and many such slices are put  
 211 together as a function of time to produce brightness variations of an observed atmospheric phenomenon over  
 212 time. A keogram is commonly used to demonstrate a presence or absence of aurora in all-sky images. In the  
 213 present study, based on the manual careful inspection of 6200 images suitable for scientific analysis, we have  
 214 selected horizontal pixel lines in the range of 3000-3400 pixels (counting along the Y-axis from the top of the

215 image) at which NLC preferred to appear. These pixels correspond to a distance of about 315-583 km from the  
 216 gondola position, when looking along the central line of the image. The image coordinates are present in Fig. 3b.  
 217 These pixels were summed to produce an integrated brightness for every column between 3000 and 3400 pixels.  
 218 The mean value and its standard deviation (std) were then calculated for the given slice along the X-axis of the  
 219 image. We have separately estimated the mean brightness and its standard deviation for each image, thus the  
 220 obtained values are independent of time and camera azimuth. Next, a selection rule was applied: brightness  
 221 values greater than 1 std of the mean were selected to classify the given slice as NLC present or absent. Then the  
 222 keogram was created by putting together slices of about 6200 images (Fig. 5), demonstrating nearly continuous  
 223 presence of NLC, that is discussed in detail in Section 4. This automatic keogram procedure fits well with the  
 224 manual procedure (described above) in identifying the presence or absence of NLC as a function of time. The  
 225 time intervals of the absence of NLC are indicated by red arrows that coincide with the manual and automatic  
 226 procedure.



227  
 228 **Figure 5: Keogram compiled from about 6200 images during the TRANSAT balloon flight on 22-26 June**  
 229 **2024. The red arrows mark four time intervals (white-grey areas) when NLC were absent. Corresponding**  
 230 **local solar times (LST) are shown for four time intervals on the x-axis. LST are calculated for the gondola**  
 231 **position, but not for the observed NLC. The number of Y-pixels is equal to 401 for which the keogram was**  
 232 **constructed.**

### 233

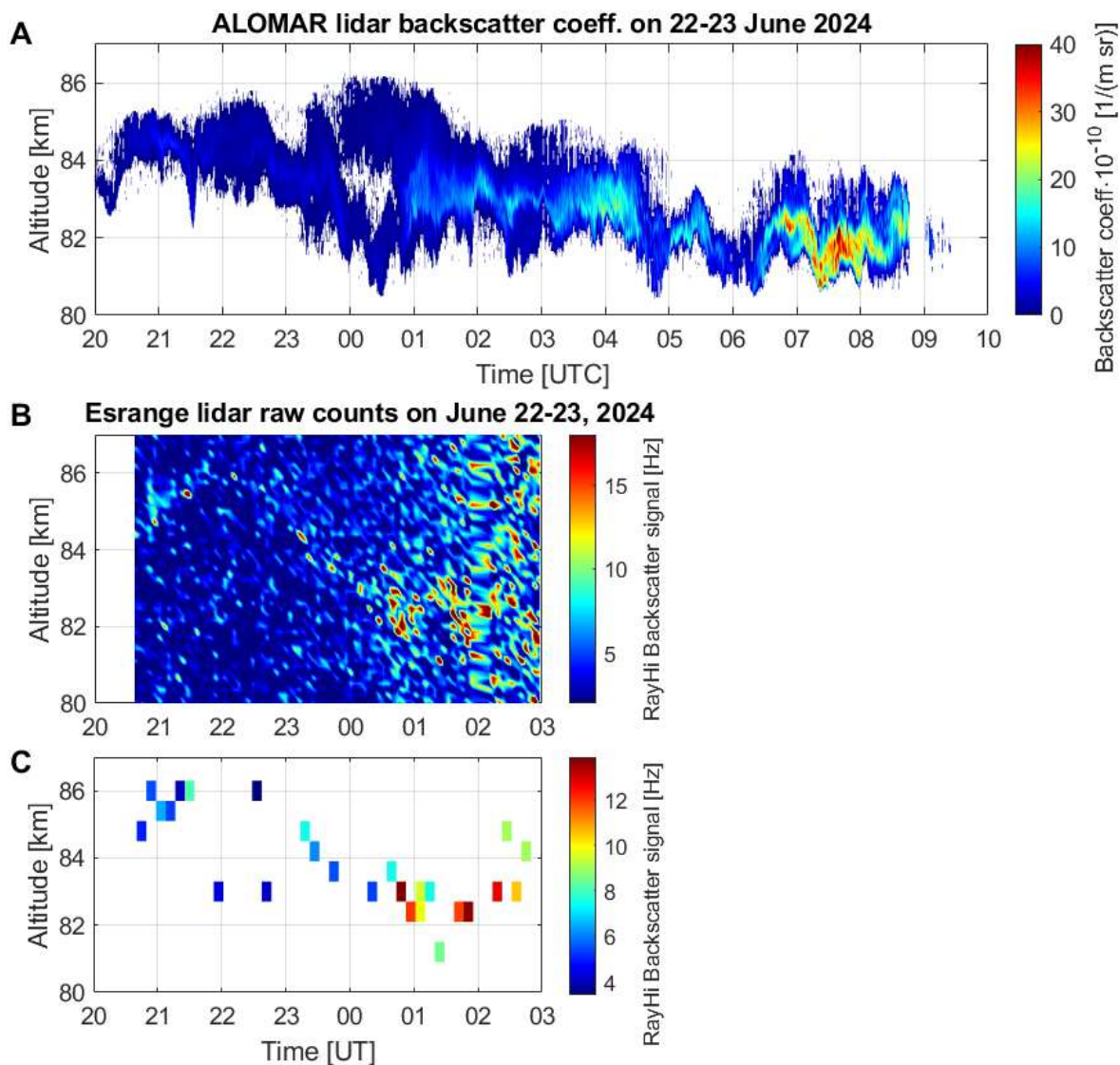
## 234 3 Ground-based and space complementary measurements

### 235 3.1 Lidar measurements

236 During the initial phase of the TRANSAT balloon flight, complementary lidar measurements were  
 237 performed at Erange (67.8°N, 21.1°E, Sweden) and Andøya (69.3°N, 16.0°E, Norway), with the aim to provide

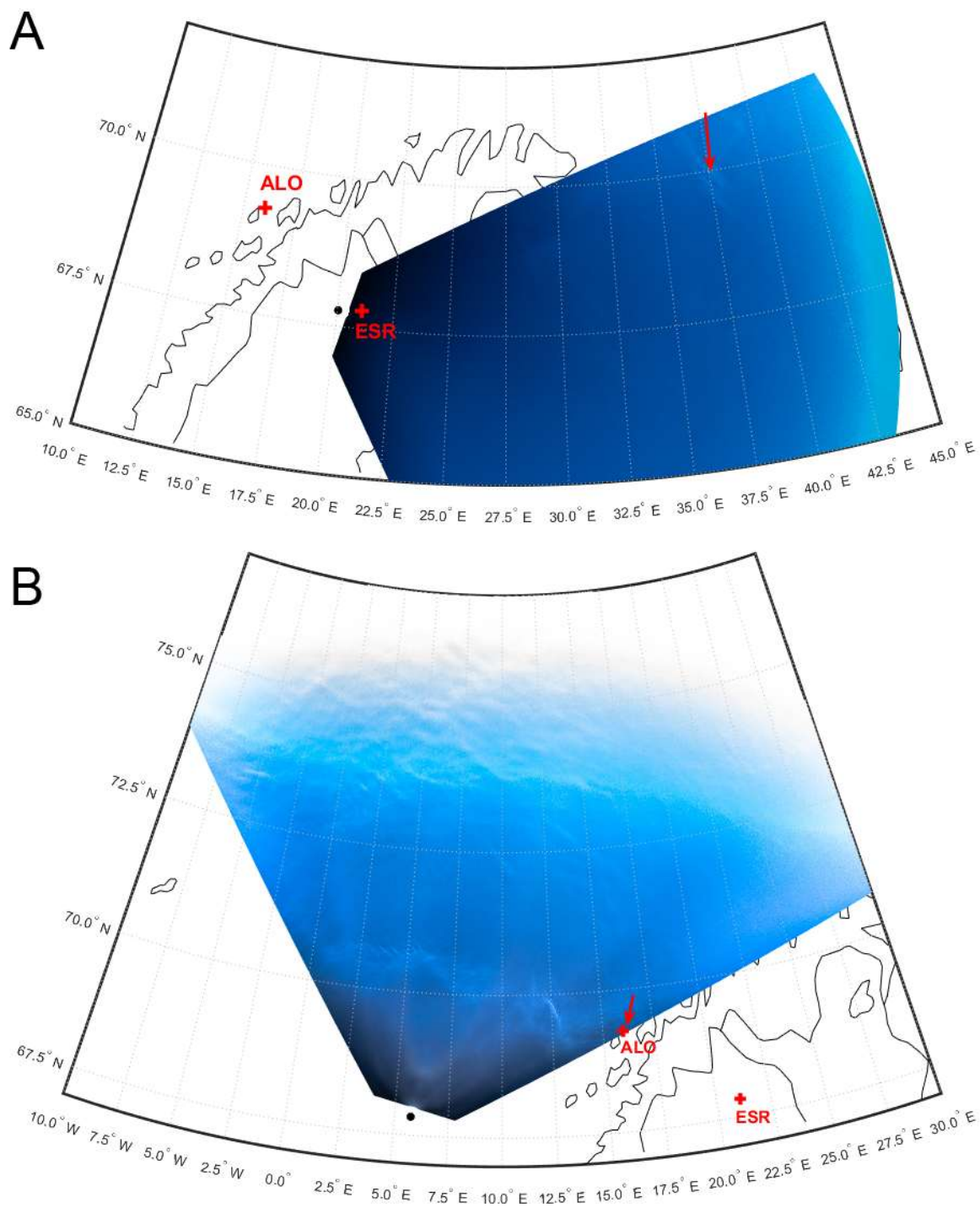
238 simultaneous and common volume (or in proximity) measurements of NLC layers above northern Scandinavia.  
239 At Esrange, we use a Rayleigh/Mie/Raman (RMR) backscatter lidar developed by the Bonn University to  
240 monitor aerosols in the troposphere, stratosphere and mesosphere as well as to determine temperature profiles in  
241 the aerosol-free part of the atmosphere (Blum and Fricke, 2005). The vertical and time resolution of the obtained  
242 measurements by the Esrange lidar is 150 m and 4.4 min, respectively. At Andøya, we use an RMR-lidar which  
243 has been operated as part of the Arctic Lidar Observatory for Middle Atmosphere Research (ALOMAR). Using  
244 measurements of the ALOMAR lidar one can study temperatures and winds in the middle atmosphere, aerosol  
245 layers in the stratosphere, polar stratospheric clouds in the lower stratosphere in winter and noctilucent clouds in  
246 the mesopause region in summer (Baumgarten, 2010). We use lidars backscattered signals from the 532-nm  
247 wavelength channel to measure NLC over Esrange and Andøya during the TRANSAT flight over northern  
248 Scandinavia. The vertical and time resolution of the obtained measurements by the ALOMAR lidar is 40 m and  
249 30 s, respectively.

250 The results of the lidar measurements during the initial phase of the TRANSAT flight are shown in Fig. 6.  
251 The NLC layer is seen in both lidar measurements between 81 and 86 km altitude from 20:30 UTC on 22 June  
252 until 01:00 UTC on 23 June. Figure 6b shows raw Esrange lidar counts and Fig. 6c represents the filtered lidar  
253 data in the following way. All Esrange lidar data were averaged over a 600 m altitude interval and a 9-minute  
254 time interval. Then the atmospheric background was estimated as the average value, and its standard deviation,  
255 of the lidar raw counts between 80 and 87 km for each time-averaged measurement. Counts exceeding 1.5  
256 standard deviations from the average value were then selected. Figure 6c highlights the main features of the NLC  
257 layer seen in Fig. 6b. Between 20 and 22 UTC, the NLC layer lifted up from 84 to 86 km, then it sank to about  
258 82 km between 22 UTC on 22 June and 01 UTC on 23 June as demonstrated by both lidars. After 01 UTC,  
259 Esrange lidar measurements become too noisy to distinguish the NLC signal from noise. Note that the  
260 ALOMAR lidar registered a double-layer NLC structure between 00 and 01 UTC. Another double-layer NLC  
261 structure will be discussed in section 4. These height variations of the NLC layer are due to propagating  
262 atmospheric gravity waves. Note that it is a very rare case of conducting simultaneous lidar measurements of  
263 NLC layers at Andøya and Esrange (separated by ~250 km) on both sides of the Scandinavian range. The  
264 ALOMAR lidar operated until 12 UTC on 23 June, continuously registering the enhanced NLC layer until about  
265 09:30 UTC, with height variations between 81 and 84 km. The extended NLC field was registered by the SONC  
266 imager above northern Scandinavia (not shown in figure) starting from ~22 UTC on 22 June 2024 and during the  
267 lidar measurements, thus continuously observing the NLC layer from the ground and stratosphere from evening  
268 hours on 22 June until morning hours on 23 June. Note that the comparison of the lidars measurements shown in  
269 Fig. 6 is qualitative because panels A and B are not shown in the same physical units.



270  
 271 **Figure 6: Lidar measurements at Andøya, Norway (A) and Esrange, Sweden (B) during the initial phase**  
 272 **of the TRANSAT balloon flight on 22-23 June 2024. (C) Filtered Esrange lidar data averaged over a 600**  
 273 **m altitude interval and a 9-minute time interval (see the text).**  
 274

275 Figure 7 illustrates the SONC images at 22:04:38 UTC on 22 June and at 09:34:32 UTC on 23 June, i.e., at  
 276 the beginning and end of the NLC observations by the Esrange and ALOMAR lidars. At the beginning of the  
 277 lidars measurements the NLC observed by the SONC imager were located to the east of the lidars, but at the  
 278 same latitude range (Fig. 7a). Later, the SONC imager slowly rotated in the antisolar direction, observing the  
 279 east-south-west sector of the sky, and, thus, observations of NLC in the mesopause over the lidars were  
 280 impossible. At the same time, at the very end of the ALOMAR lidar observations at about 09:30 UTC on 23  
 281 June, the SONC imager looked north-northeast and detected faint NLC at the very edge of the image frame  
 282 directly over the ALOMAR lidar (Fig. 7b). At that time, NLC were between 81.6 and 82.0 km (Fig. 6a). Thus,  
 283 lidar measurements can complement balloon-borne observations, providing information on vertical dynamics of  
 284 the NLC layer observed from the stratosphere.



285  
 286 **Figure 7: Projection of two SONC images on the Earth's surface at 22:04:38 UTC on 22 June 2024 (A)**  
 287 **and at 09:34:32 UTC on 23 June 2024 (B) during the TRANSAT balloon flight. The black dot denotes the**  
 288 **balloon position. The red crosses are the position of the ALOMAR (ALO) and Esrange (ESR) lidars. The**  
 289 **red arrows show the locations of NLC.**

290

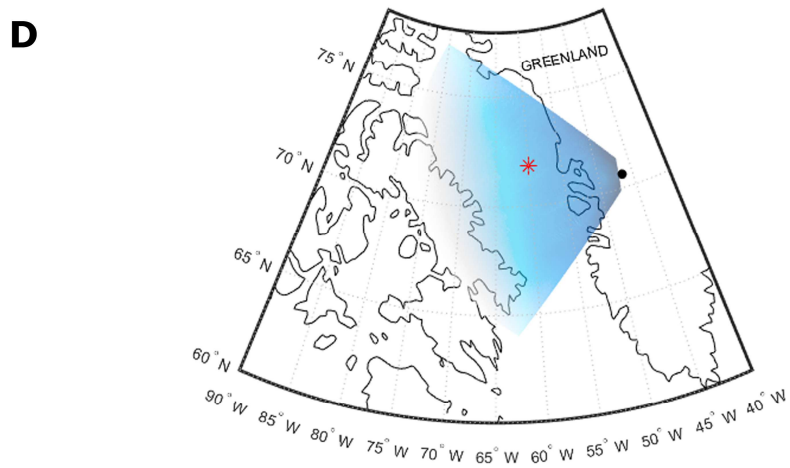
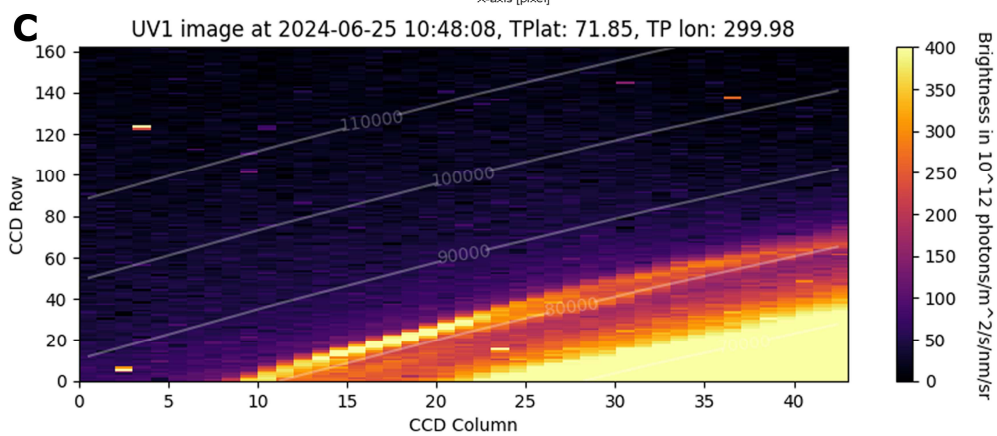
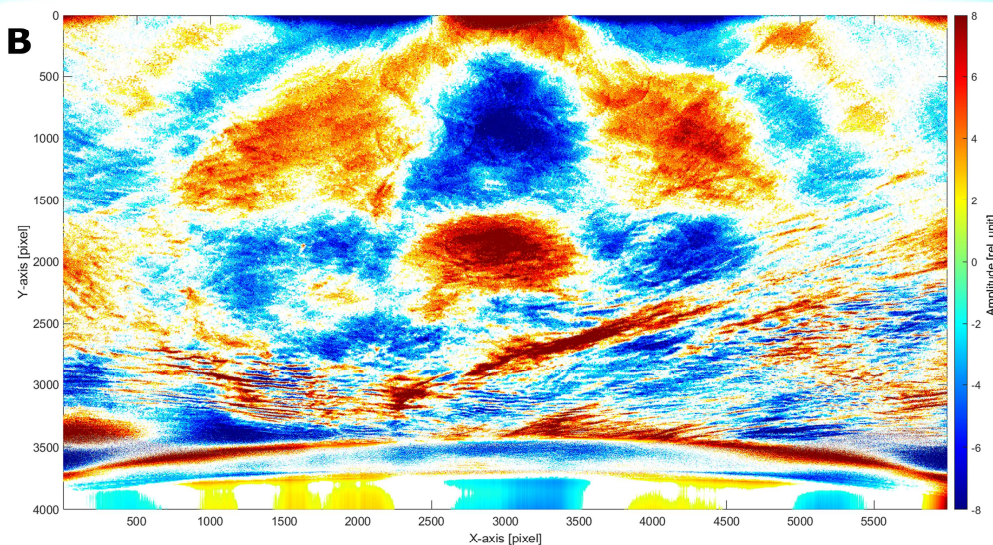
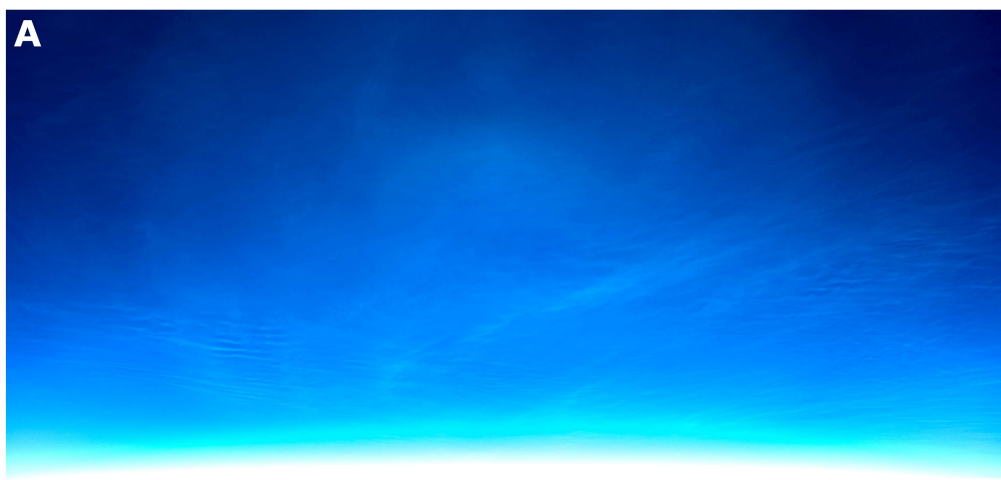
291

### 3.2 Space measurements

292 During the TRANSAT flight, measurements of PMC from space were also conducted with the MATS  
293 satellite. MATS (Mesospheric Airglow/Aerosol Tomography and Spectroscopy) is a Swedish satellite mission,  
294 launched in November 2022, designed to investigate polar mesospheric clouds, temperature regime and  
295 atmospheric gravity waves in the mesosphere (Gumbel et al., 2020). The MATS satellite utilizes airglow  
296 emissions coming from excited molecular oxygen in the near infrared range of the spectrum (760-780 nm, the O<sub>2</sub>  
297 (0-0) A-band) as well as scattered light from PMC in the ultraviolet (270 and 340 nm). The primary scientific  
298 instrument on-board the satellite is the limb imager, a telescope with six wavelength channels that continuously  
299 captures images of the atmospheric limb with a field of view of about 40 km in the vertical and 250 km across  
300 track at the tangent point. The horizontal and vertical resolution of MATS limb images is 5.7 km and 290 m,  
301 respectively. The horizontal resolution is consistent with AIM/CIPS images (Randall et al., 2017) and the  
302 vertical resolution of 290 m should be considered high for satellite missions. Using a tomographic analysis of  
303 acquired MATS images, one can reconstruct waves in three dimensions and provide 3-dimensional fields of  
304 airglow, PMC properties and temperature (Megner et al., 2025).

305 Figure 8 demonstrates an example of MATS images in the UV channel 1 at 270 nm taken at 10:48:08 UTC  
306 on 25 June 2024. This measurement was done at the tangent point in the mesopause close to the west coast of  
307 Greenland as illustrated in Fig. 8d. One can clearly see the presence of the PMC layer in Fig. 8c as the bright  
308 yellow band on the atmospheric limb between 80 and 85 km tangent altitude. The time and location of the PMC  
309 by MATS agree very well (time difference of 6 seconds) with the NLC observation obtained from the  
310 TRANSAT balloon, with the MATS tangent point being in the field of view of the SONC imager as seen in Fig.  
311 8d. Such simultaneous common-volume observation of NLC from the stratosphere and space was made for the  
312 second time; the first one was made by the PMC Turbo stratospheric flight and the AIM satellite in July 2018  
313 (Fritts et al., 2019). But in the present study this was done for the first time when such a large-scale NLC/PMC  
314 field (extending at least 1500 km from north to south) was seen from the stratosphere and from space based on  
315 the limb-viewing observation using the MATS satellite. Note that MATS also detected NLC in the next orbit  
316 over Greenland and in field of view of the SONC imager at 12:22:16 UTC on June 23 (not shown in figure). In  
317 the present study, we do not aim to completely compare all possible NLC observations from the stratosphere and  
318 the MATS satellite, but to demonstrate the fundamental possibility of such observations in one figure only. Thus,  
319 MATS observed an extended PMC layer in a large volume of the mesopause at least over Greenland, Baffin Bay  
320 and Baffin Island. Part of this large-scale NLC field was registered from the stratosphere by the SONC imager  
321 shown in Fig. 8a. Figure 8b demonstrates a 2D-filtered image with a second-order polynomial removed from the  
322 original image (see section 2.3), which shows NLC modulations due to gravity waves of various scales  
323 throughout the lower part of the image. At the same time, images taken from the stratosphere have much higher  
324 spatial resolution, showing small- and medium-scale wave dynamics (including smaller gravity waves and  
325 turbulent structures) that MATS cannot resolve using the limb-viewing geometry. Thus, studies of spatial-  
326 temporal variability of NLC/PMC can be carried out simultaneously from the stratosphere and space,  
327 complementing each other.

328



330 **Figure 8: Example of NLC measurements obtained from the stratosphere and space on 25 June 2024**  
 331 **during the TRANSAT balloon flight. (A) Image, taken by the SONC imager at 10:48:02 UTC, shows the**  
 332 **extended NLC field covering almost the whole image area. (B) 2D-filtered image with a second-order**  
 333 **polynomial removed from the original image shown in A (see the text). (C) Image, taken by the MATS**  
 334 **satellite at 10:48:08 UTC, illustrate part of the atmospheric limb, with the bright yellow PMC layer seen**  
 335 **between 80 and 85 km. Data are shown for the UV channel 1 at 270 nm. (D) Projection of the NLC image**  
 336 **shown on Panel A onto the Earth's surface. The black dot is the position of the TRANSAT balloon, the**  
 337 **red asterisk marks the MATS tangent point which is in the field of view of the SONC imager.**

338

## 339 4 Results and Discussion

### 340 4.1 Nearly continuous observations of NLC

341 The first scientific result is the nearly continuous presence of mesospheric clouds in the observed latitude  
 342 range of 60–75°N during 3.8 days of the TRANSAT balloon flight. In total, there were four intervals of NLC  
 343 disappearances as shown by the blue circles in Fig. 2a and by the red arrows in Fig. 5. These events occurred on  
 344 23 June at 09:30–10:50 UTC on 23 June, at 18:20–21:20 UTC on 24 June, at 17:45–02:40 UTC on 25-26 June,  
 345 and at 09:00–11:00 UTC on 26 June. Outside these intervals, NLC were continuously observed, often with  
 346 varying brightness and wave modulation.

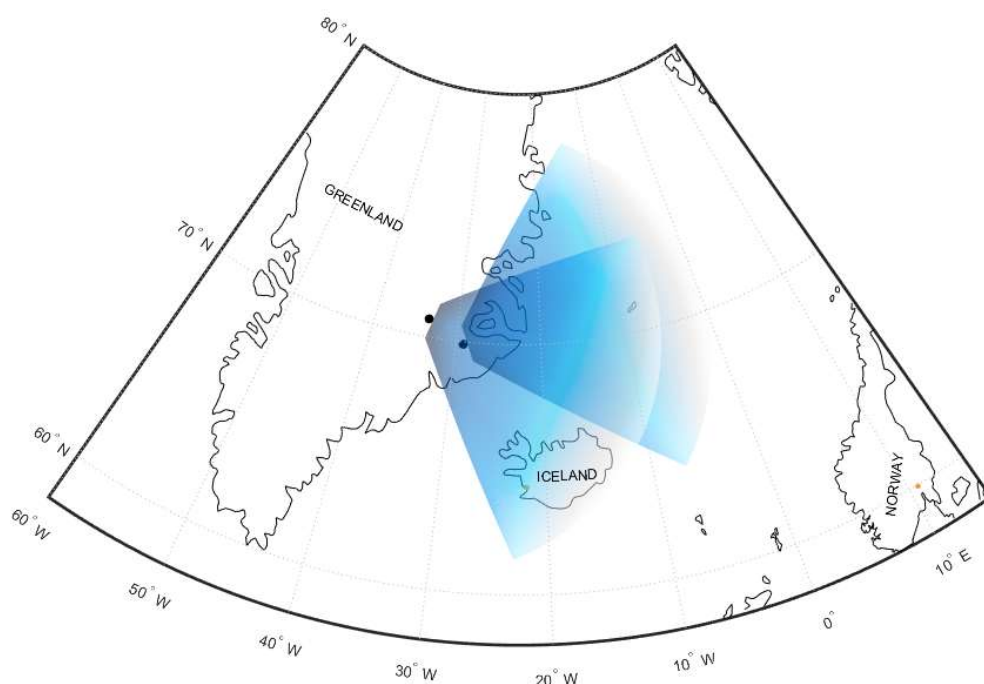
347 These NLC disappearances are not related to local solar time (see four local solar time intervals on the x-axis  
 348 in Fig. 5). That is, these NLC interruptions were of a rather spontaneous nature and were not related to solar  
 349 thermal tides, which are regular atmospheric variations. Indeed, Fritts et al. (2019) demonstrated more or less  
 350 regular NLC disappearances in the evening (18-24 LST) and morning hours (6-12 LST), observed during the  
 351 PMC Turbo balloon flight from Sweden to Canada in July 2018. The authors associated this with solar  
 352 semidiurnal and diurnal thermal tides in the polar summer mesopause, the amplitudes of which reach 10-20 K,  
 353 which is comparable to ones by gravity waves in the mesopause region (Rapp et al., 2002). It should be noted  
 354 that this result was obtained on the basis of lidar measurements on the PMC Turbo balloon, that is, obtained with  
 355 a very small field of view of a few meters in the mesopause. Therefore, for such a small volume of the  
 356 mesopause one can expect the dominant influence of large-scale waves such as solar tides. Note that continuous  
 357 lidar observations at 69°N demonstrate strong NLC diurnal variations due to solar tides, with a maximum  
 358 occurrence frequency of about 65% in the morning hours and a minimum of about 35% around noon (Fiedler et  
 359 al., 2011). In the case of the TRANSAT balloon flight NLC observations were carried out on large scales of  
 360 about 1000-1500 km at a time. At such large scales, not only solar tides manifest themselves but also  
 361 propagating gravity waves of various scales from 1 to 1000 km. Indeed, a typical picture seen from the  
 362 stratosphere was that we saw a disappearance of NLC in one area of the mesopause (for example, in the eastern  
 363 part), but simultaneous appearance of other NLC in another part of the mesopause (for example, in the western  
 364 part). In other words, large-scale NLC fields were generally represented by numerous wavy patterns of sporadic  
 365 nature. One can assume that gravity waves, continuously coming from the lower atmosphere, form a new NLC  
 366 and/or modulate an existing NLC layer in different parts of the mesopause (as observed in the present  
 367 experiment), thereby dominating solar thermal tides on large scales. At the same time, we should note that this  
 368 result was obtained on the basis of a single 3.8-day flight and a limited range of latitudes (60-75°N) and

369 longitudes (45°E-95°W). That is why the present case study cannot claim to be a general statement about the  
 370 relative importance of solar tides compared to gravity waves.

371

#### 372 4.2 A case study of the NLC disappearance

373 The second result is connected to the disappearance of NLC at 18:20-21:20 UTC (16:23-19:06 LST) on 24  
 374 June 2024 (Fig. 5). This NLC disappearance was observed over the Atlantic Ocean near the east coast of  
 375 Greenland and over Iceland as demonstrated in Fig. 9.



376

377 **Figure 9: Projection of the field of view of the SONC camera on the Earth's surface at 18:20 UTC (16:23**  
 378 **LST) and 21:20 UTC (19:06 LST) on 24 June 2024, when no NLC were observed from the stratosphere.**  
 379 **The black dots mark the position of the TRANSAT balloon.**

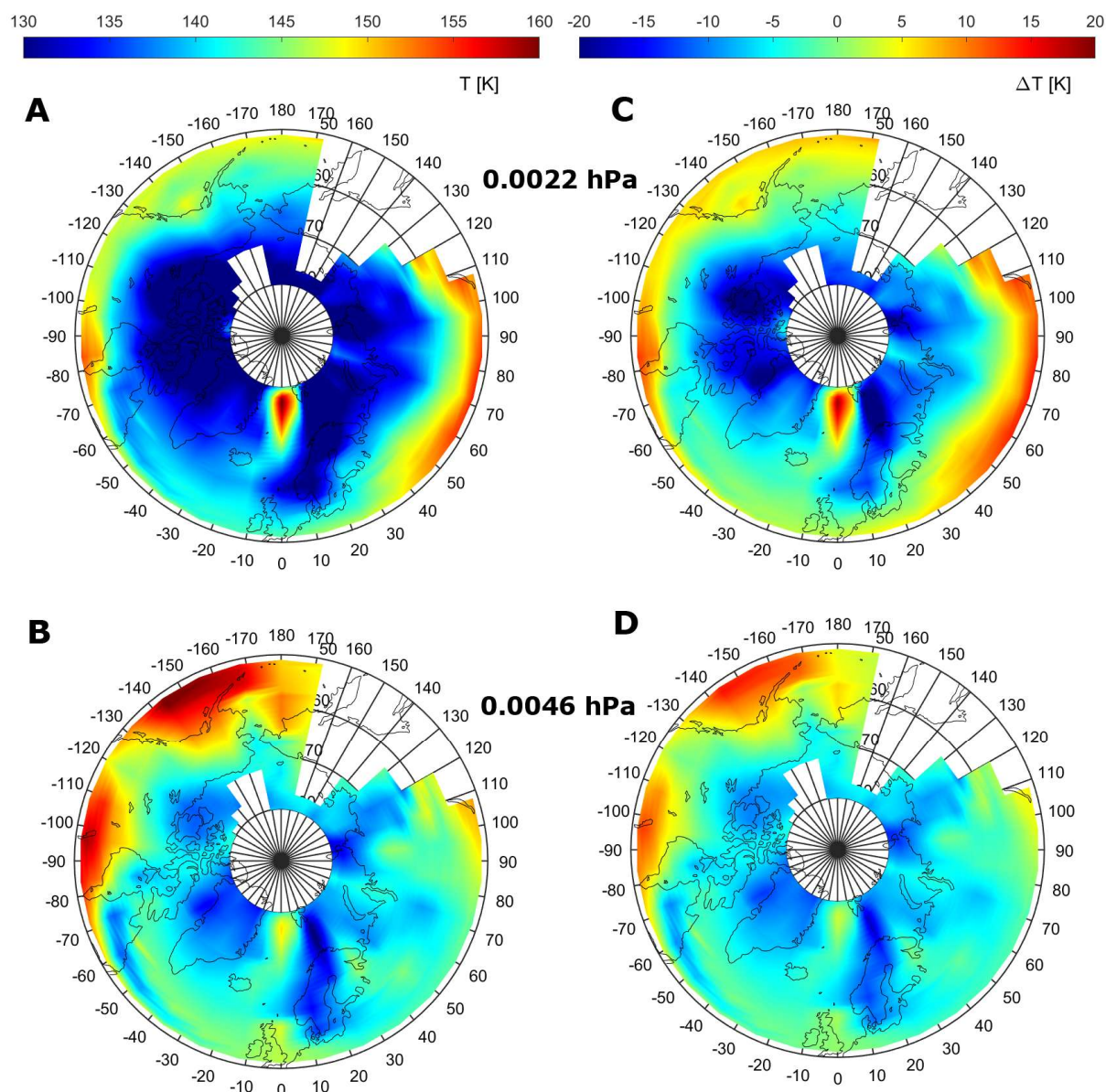
380

381 We have tried to find out the reason for this NLC disappearance. For this data of the Aura/MLS temperature  
 382 and water vapor measurements have been used to obtain a comprehensive picture of the mesopause environment  
 383 in the region of interest. Aura/MLS temperature and water vapor measurements of ver.5.0 and level 2 data  
 384 quality were obtained from the NASA public web-site:

385 [https://acdisc.gesdisc.eosdis.nasa.gov/data/Aura\\_MLS\\_Level2/](https://acdisc.gesdisc.eosdis.nasa.gov/data/Aura_MLS_Level2/). According to the Aura/MLS data quality and  
 386 description document (version 5.0x level 2 and 3), for Aura/MLS temperature measurements, the vertical  
 387 resolution in the mesopause region is 11 km at 0.01 hPa (~80 km) and 12 km at 0.001 hPa (~90 km). The

388 horizontal resolution (along track) is ~250 km at 0.01 hPa and ~280 km at 0.001 hPa. The pressure range  
389 recommended for scientific use is from 261 hPa (~10 km) to 0.00046 hPa (~93 km). Typical precisions for  
390 individual Aura/MLS temperature profiles at this altitude range are  $\pm 3.4$ – $3.6$  K. For Aura/MLS water vapor  
391 measurements, the vertical resolution is 8.8 km at 0.01 hPa and 10.3 km at 0.002 hPa. The horizontal resolution  
392 is ~725 km at 0.01 hPa and ~350 km at 0.002 hPa. The pressure range recommended for scientific use is from  
393 316 hPa to 0.001 hPa. Typical precisions for individual Aura/MLS water vapor profiles are 55% at 0.01 hPa and  
394 450% at 0.001 hPa. The description on the MLS temperature product and its validation can be found in  
395 Froidevaux et al. (2006) and Schwartz et al. (2008). The validation of water vapor data is described in detail by  
396 Read et al. (2007) and Lambert et al. (2007). The frost point temperature in the mesopause was calculated using  
397 Aura/MLS water vapor data based on thermodynamics of the vapor pressure of ice (Murphy and Koop, 2005).

398 The results are shown in Fig. 10 demonstrating the following peculiar feature. A prominent localized warm  
399 area in the mesopause region at the pressure levels of 0.0022 hPa (about 86 km geometrical height) and 0.0046  
400 hPa (about 83 km) was present between Greenland and Scandinavia, with temperatures 20-30 K higher than  
401 those in the adjacent mesopause regions at 0.0022 hPa. The location of this warm spot coincides well with the  
402 position of the mesopause visible from the TRANSAT balloon when no NLC were seen (Fig. 9). The right  
403 column in Fig. 10 shows the differences between the actual temperature measurements and the frost point  
404 temperature as calculated using Aura/MLS water vapor measurements, with positive temperature differences  
405 being as much as 10-15 K in the center of this warm spot. We double-checked all the Aura/MLS data  
406 (temperature and water vapor) which show good quality data suitable for scientific analysis and we could not  
407 find any error in these data.



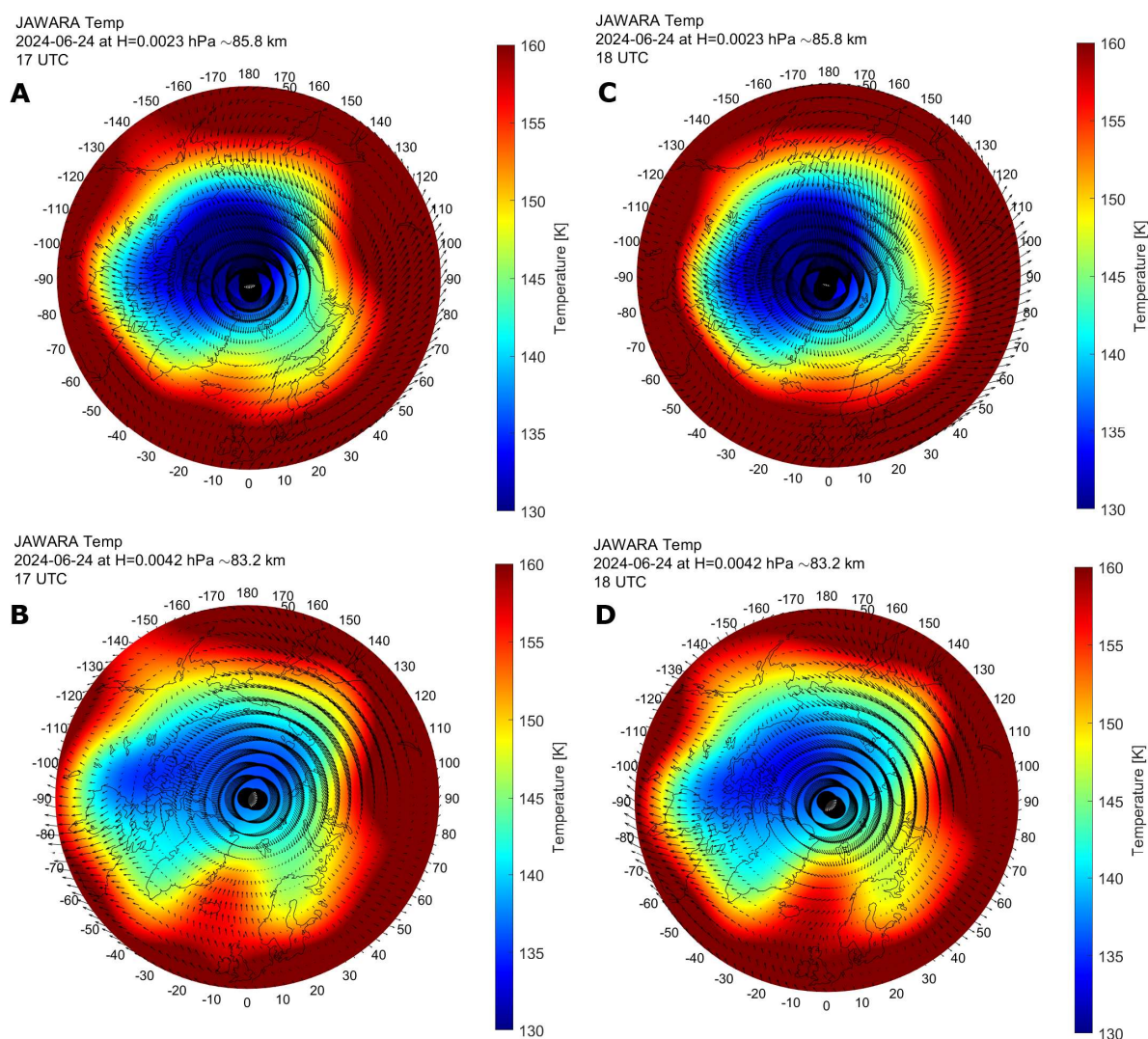
408  
 409 **Figure10: (A) Aura/MLS temperature measurements at the pressure level of 0.0022 hPa (~86 km) and (B)**  
 410 **at 0.0046 hPa (~83 km) on 24 June 2024. Differences between the temperature and the frost point**  
 411 **temperature as estimated based on Aura/MLS water vapor measurements at 0.0022 hPa (C) and 0.0046**  
 412 **hPa (D), see the text.**

413  
 414 In Fig. 10 (especially in plots for the 0.0046 hPa level), one can note that the warm local region at high  
 415 latitudes was an extension of a warm vast area located at mid-latitudes. That is, one can assume that this local  
 416 warm region was caused by a jet of warm air mass from middle latitudes to high latitudes. To test this  
 417 hypothesis, we apply the Japanese Atmospheric General circulation model for Upper Atmosphere Research Data  
 418 Assimilation System (JAGUAR-DAS), which is a data assimilation system for the whole neutral atmosphere  
 419 (Koshin et al., 2020; 2022). Specifically, JAGUAR-DAS Whole neutral Atmosphere Reanalysis (JAWARA) has  
 420 been considered in the present study. JAWARA is a long-period reanalysis, starting from September 2004,  
 421 which covers the altitude range from the surface to the lower thermosphere (~110 km). The vertical resolution of  
 422 JAWARA data in the mesopause region between 80 and 90 km is about 0.7 km. JAWARA outputs, distributed

423 on a horizontal grid spacing of  $2.81^\circ$ , include the following hourly data: temperature, zonal, meridional and  
 424 vertical wind velocities, geopotential height, temperature tendency due to diabatic heating, zonal and meridional  
 425 forcing from the GW parameterization (Koshin et al., 2025). Note that JAWARA assimilates MLS temperature,  
 426 meaning that the temperature fields in MLS and JAWARA are not fully independent and the mutual agreement  
 427 might be expected because of the data assimilation.

428 JAWARA temperature and neutral wind data in the mesopause region are shown on 24 June 2024 in Fig. 11,  
 429 demonstrating the following features. The warm localized spot was present between Greenland and Scandinavia,  
 430 and it was most pronounced at 0.0042 hPa,  $\sim 83$  km, (lower plots), which agrees well with the position of the  
 431 warm spot represented by Aura/MLS. At the same time, wind velocity vectors show that the local wind jet was  
 432 formed, which moved from middle to high latitudes in the region with this warm spot. Thus, this warm spot in  
 433 the mesopause was caused by the intrusion of a warm air mass from the middle to high latitudes between  
 434 Greenland and Scandinavia. This warm spot induced sublimation of ice particles in the mesopause, which caused  
 435 NLC to disappear during the TRANSAT balloon flight over the North Atlantic and the east coast of Greenland in  
 436 the evening of 24 June 2024. The mechanism of this air intrusion from middle to high latitudes is beyond the  
 437 scope of the present paper.

438



439

440

441 **Figure 11: JAWARA model temperature (color code) and neutral wind velocity vectors (arrows) on 24**  
 442 **June 2024. The data are shown at the pressure level of 0.0023 hPa (A and C) and at 0.0042 hPa (B and D),**  
 443 **and at 17:00 UTC (A and B) and at 18:00 UTC (C and D).**

444

445 In general, the relationship between NLC occurrence and ambient mesopause temperature is known. Berger  
 446 and von Zahn (2002), using model studies with a 3-D general circulation model of the middle atmosphere  
 447 (COMMA/IAP), demonstrated that the saturation ratio  $S=1$  closely coincides with a temperature of 147 K at 83  
 448 km altitude at any latitude poleward of  $65^{\circ}\text{N}$ . If the air is supersaturated ( $S>1$ ), this condition allows ice particles  
 449 to exist in the summer mesopause region between 83 and 93 km, depending on latitude. A similar experimental  
 450 result on the mesopause temperature was found by Dalin et al. (2011), who analyzed Aura/MLS temperatures  
 451 and NLC occurrences observed from the ground around the globe. The authors found that MLS temperatures  
 452 around the mesopause control the NLC climatology, i.e., a drop in temperature below the frost point temperature  
 453 in June corresponds to the beginning of the NLC season, and an increase in temperature above the frost point  
 454 temperature in August determines the end of the NLC season. The mesopause frost point temperature was  
 455 estimated to be in the range of 145 to 147 K, with water vapor contents varying between 3.5 and 6.0 ppmv.  
 456 Hervig et al. (2015), analyzing NLC observations from space using AIM/SOFIE, found that NLC variations are  
 457 dominated by the mesopause temperature, but a combination of temperature and water vapor content provides  
 458 the best description of ice water content in the Northern Hemisphere mesopause. At high latitudes, Fiedler et al.  
 459 (2011) found a strong anticorrelation (-0.96) between LIMA model temperatures and diurnal NLC occurrences  
 460 above ALOMAR ( $69^{\circ}\text{N}$ ). At middle latitudes, Gerding et al. (2013) found anticorrelations in the range of  $-0.76 \div$   
 461  $-0.85$  (depending on altitude) between the NLC occurrence rate and mesopause temperature using lidar  
 462 measurements at K hlungsborn ( $54^{\circ}\text{N}$ ). We should note that the present case study demonstrates not only the  
 463 well-known link between increased temperature and NLC absence, but more importantly, the intrusion of a  
 464 warm air mass from the middle to high latitudes in the mesopause region. The latter phenomenon is poorly  
 465 studied and rarely found in the literature.

466

### 467 **4.3 A double-layer structure in NLC**

468 The third early result addresses a double-layer event in NLC observed over Greenland on 25 June 2024. The  
 469 reader is recommended to look at the video of NLC image sequence at 05:08-06:49 UTC (02:35-04:08 LST) on  
 470 25 June (<https://doi.org/10.7910/DVN/AKJK4P>). One can see at least two NLC layers moving in opposite  
 471 directions: one cloud layer visually moved approximately from the top to the bottom of the image frame,  
 472 whereas another cloud layer moved in the opposite direction from the bottom to the top. Double-layer and  
 473 multiple-layer structures in NLC/PMC have been previously observed and modeled in a number of studies  
 474 (Baumgarten et al., 2012; Dubinskii and Popel, 2012; Kaifler et al., 2013; Gao et al., 2017; Li et al., 2017).

475 We have carefully estimated speeds and directions of seven individual NLC points in each of these two  
 476 different layers. NLC point trace analysis was applied to the original (unfiltered and unprojected) images. After  
 477 completing the trace analysis, the estimation of NLC velocities (speeds and directions) was performed on  
 478 projected images. The results of this analysis are as follows. For the NLC layer visually moving from the bottom  
 479 to the top, the average NLC speed was about 28 m/s, with the average azimuth of about  $18^{\circ}$  (counting clockwise

480 from the north). For the NLC layer moving from the top to the bottom, the average NLC speed was about 60  
 481 m/s, with the average azimuth of about  $193^\circ$ . These statistical results are summarized in Table 1 as well as  
 482 shown in Fig. 12, demonstrating NLC velocity vectors (green and yellow arrows) estimated for the two different  
 483 layers. Note that we have taken into account the velocity vector of the TRANSAT flight (zonal and meridional  
 484 speed was  $-10.5$  m/s and  $-7.1$  m/s, respectively) when calculating these NLC wind velocities vectors. To  
 485 calculate NLC speeds, the average height of the entire cloud layer was chosen as 83 km. Uncertainty in the  
 486 height of the NLC layers between 82 and 86 km gives an error of 3-4% of the average NLC speed.

487 It can be assumed that different movements of the two NLC layers were caused by different wind systems  
 488 located at different heights in the mesopause region. We cannot measure the heights of the different NLC layers  
 489 but we can consider a model simulation to check this assumption. We utilize JAWARA zonal and meridional  
 490 wind data in the mesopause region taken at 06:00 UTC on 25 June 2024, i.e., when and where different motions  
 491 of the NLC were observed.

492 JAWARA wind data are shown in Fig. 12 by the vector field as well as by the absolute wind speed (color  
 493 code). Panel A represents JAWARA wind data at the pressure level of 0.0042 hPa ( $\sim 82.9$  km) above Greenland  
 494 and seven NLC velocity vectors (green arrows) observed in the NLC layer which was moving in the NNE  
 495 direction (visually from the bottom to the top). The average wind speed was about 21 m/s in the direction of  $13^\circ$   
 496 (counting clockwise from the north) in the vicinity of the observed NLC. Panel B illustrates JAWARA wind data  
 497 at the pressure level of 0.0017 hPa ( $\sim 86.8$  km). One can see about the opposite direction (to SSW) of the model  
 498 wind field to that shown on panel A. The average JAWARA wind speed was about 56 m/s, with the average  
 499 azimuth of  $188^\circ$ , in the vicinity of the observed NLC. Seven NLC velocity vector are shown by the yellow  
 500 arrows which have about the same speed and the direction of motion. All these statistical data are summarized in  
 501 Table 1, which demonstrate good agreement between the measured NLC and JAWARA wind velocities both in  
 502 the absolute value and in the propagation direction, taking into account their uncertainties. Note that the  
 503 JAWARA model has a low horizontal spatial resolution ( $2.81^\circ$  or  $\sim 310$  km in latitude and  $\sim 113$  km in longitude  
 504 in the analyzed space domain over Greenland) and cannot reproduce wave dynamics due to small-scale gravity  
 505 waves. However, in this particular case, the JAWARA model does correspond well to the observed motions of  
 506 the two different NLC layers.

507

508 **Table 1.** Statistical parameters of the movement of two different layers observed in NLC during the TRANSAT  
 509 balloon flight on 25 June 2024. For comparison, wind data from the JAWARA model are shown. Uncertainties  
 510 represent one standard deviation.

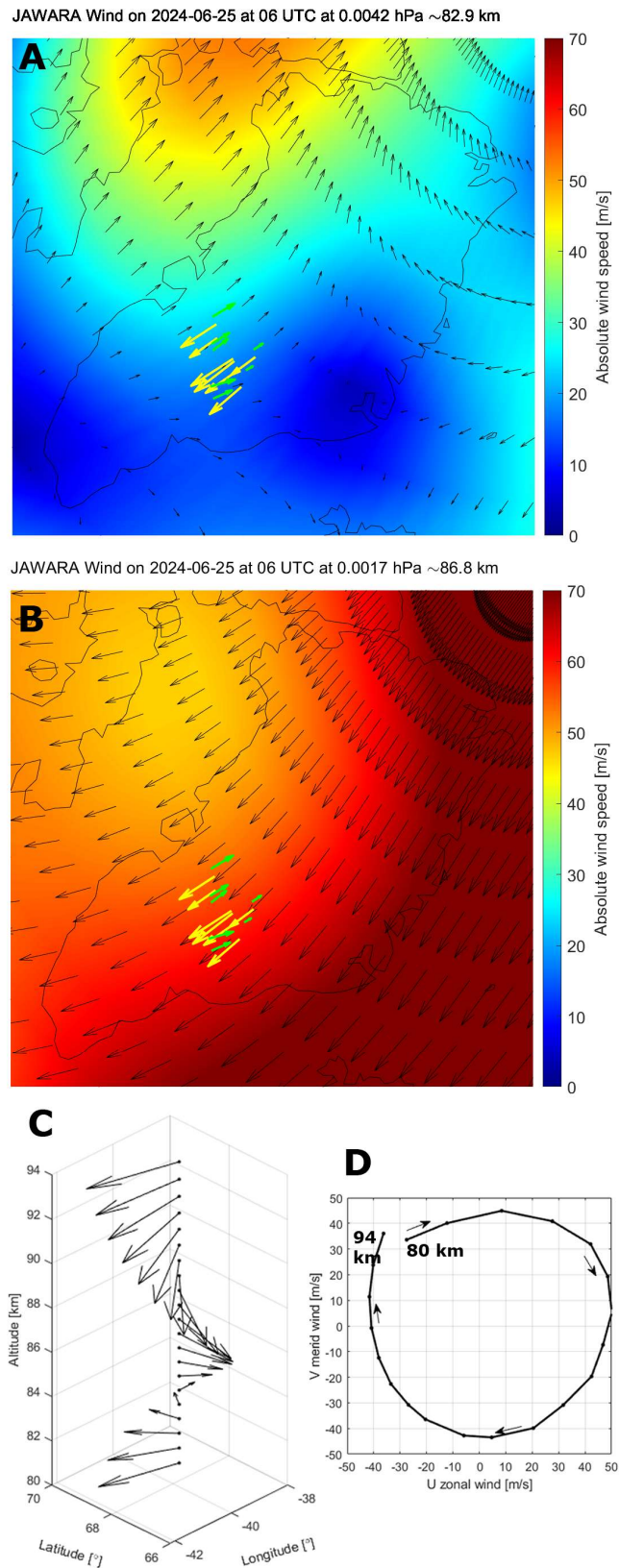
Two NLC layers oppositely moved in image frame	NLC speed (m/s)	NLC azimuth (degree from north)	JAWARA wind speed (m/s)	JAWARA wind azimuth (degree from north)
From bottom to top	$27.8 \pm 10.0$	$18.2 \pm 8.2$	$21.0 \pm 3.7$ at 0.0042 hPa	$13.0 \pm 12.0$ at 0.0042 hPa
From top to bottom	$60.5 \pm 11.3$	$192.5 \pm 2.2$	$56.1 \pm 2.5$ at 0.0017 hPa	$188.0 \pm 4.3$ at 0.0017 hPa

511

512 Panel C of Fig. 12 shows the JAWARA wind velocity vector as a function of altitude for a specific point in  
 513 the vicinity of the observed NLC. The cyclic rotation of the wind velocity vector is clearly seen between 80 and  
 514 94 km altitude, i.e., there was a circular rotation of the wind vector along the azimuth of  $360^\circ$ . Panel D illustrates

515 the corresponding hodograph of the tip of the horizontal wind vector with the subtracted mean velocity values (-  
516 33 m/s and -18 m/s for the zonal and meridional wind component, respectively) between 80 and 94 km, that is,  
517 perturbations of the horizontal wind velocity. It is well known that a gravity wave induces horizontal wind  
518 variations rotating, in general, elliptically with height, and hodograph analysis is commonly used to derive  
519 gravity wave parameters (Gossard and Hooke, 1975; Eckermann, 1996 and references therein). In the present  
520 case, the hodograph has an almost circular form, implying near circular polarization ( $P \approx 0$ ). Perturbations of the  
521 horizontal wind are of 45-50 m/s, and the perturbation vector has a clockwise rotation with increasing height  
522 which means that the group velocity of this particular gravity wave was propagating upward (phase velocity was  
523 downward). Such an inertia-gravity wave could indeed generate winds in different directions in the given  
524 volume of the mesopause, forming a multiple-layer structure from a single NLC layer. The inertia-gravity wave  
525 interpretation is a plausible scenario which is consistent with JAWARA winds and NLC motions. At the same  
526 time, it should be noted that the background wind in the mesopause region abruptly changes its speed and  
527 direction with altitude in summer (Portnyagin and Solovjova, 2000; Conte et al., 2025). Therefore, other  
528 mechanisms such as the vertical displacement of the NLC layer by gravity waves, may provide the observed  
529 different NLC motions.

530 It is important to note the following. The clockwise wind rotation with altitude by JAWARA was the  
531 opposite of that found by Conte et al. (2025), who have analyzed long-term meteor radar measurements in the  
532 mesopause region at high latitudes over northern Norway. The authors have obtained the counter-clockwise  
533 rotation of the mean wind speed with altitude in the summer time. The same effect of the wind rotation with  
534 altitude is predicted by the global empirical wind model for the upper mesosphere/lower thermosphere  
535 (Portnyagin and Solovjova, 2000). In this present case, the clockwise rotation of the wind speed indicates the  
536 dominance of the inertia-gravity wave over the mean wind rotation speed in the space-time domain under  
537 consideration. Also, we should note that even without inertia-gravity waves, winds in the mesopause region can  
538 rotate with altitude (Ekman spiral) under the action of the Ekman-type mechanism involving Coriolis force and  
539 turbulent viscosity (Chkhetiani and Shalimov, 2010; 2022).



540

541 **Figure 12: JAWARA wind data (thin black arrows) at the pressure level of 0.0042 hPa, ~82.9 km (A) and**542 **at the pressure level of 0.0017 hPa, ~86.8 km (B) at 06 UTC on 25 June 2024. The color code is the**543 **absolute horizontal wind speed. The green and yellow arrows show velocities of NLC moving in opposite**544 **directions (see the text). (C) JAWARA wind velocity vector selected for a specific location (68.4°N,**

545 **39.4°W) as a function of altitude between 80 and 94 km. (D) Hodograph of disturbances of the horizontal**  
 546 **wind velocity vector between 80 and 94 km. The thin arrows show the direction (clockwise rotation) of**  
 547 **wind velocity disturbances with altitude.**

548

## 549 **5 Conclusions**

550 Observations of noctilucent clouds were performed from the stratosphere during the TRANSAT transatlantic  
 551 long-duration balloon flight between Sweden and Canada on 22-26 June 2024. NLC were observed with the  
 552 SONC imager composed of three high-resolution SONY  $\alpha 7$  Mark III cameras, stabilized on the TRANSAT  
 553 gondola. NLC cannot be detected by an imager from the ground during the midnight Sun season due to strong  
 554 background scattering in the lower atmosphere. However, an observation from the stratosphere can detect NLC  
 555 during 24 hours. Stratospheric measurements offer a view of mesospheric cloud dynamics on small- and large-  
 556 scales, bridging the observational gap between ground-based and satellite platforms. The main results of this  
 557 study can be summarized as follows:

- 558 1. One wide-angle camera was completely operational during the whole flight for 3.8 days, taking a total of  
 559 40,000 images, of which about 6200 images are suitable for scientific analysis.
- 560 2. NLC were detected nearly continuously during the whole flight, showing a strong variability in space and  
 561 time. The dominant role of solar thermal tides in the summer mesopause decreases when NLC are observed  
 562 on large scales of about 1500 km. At such scales, gravity waves of various scales from 1 to several hundred  
 563 km play the largest role, evolving and modulating NLC layers in different regions of the polar mesopause.  
 564 Note that this result was obtained on the basis of a single 3.8-day flight and a limited range of latitudes (60-  
 565 75°N) and longitudes (45°E-95°W). Thus, the present case study cannot claim to be a general statement  
 566 about the relative importance of solar tides compared to gravity waves.
- 567 3. Ground-based support of the TRANSAT balloon campaign was represented by two lidars located at Esrange  
 568 and Andoya. Both lidars registered NLC at the time of the initial phase of the balloon flight over northern  
 569 Scandinavia. The NLC layered was continuous from 20 UTC on 22 June until 09 UTC on 23 June,  
 570 modulated in height between 81 and 86 km, and showing a double-layer structure.
- 571 4. The same mesospheric cloud layer was recorded from the stratosphere and space around noon on 25 June  
 572 2024. Such a simultaneous common-volume NLC detection was carried out, for the first time, using a limb-  
 573 geometry by the MATS satellite. The extended cloud layer was observed over at least Greenland, Baffin Bay  
 574 and Baffin Island, with part of this layer registered from the stratosphere over the west coast of Greenland  
 575 and Baffin Bay. Images from the stratosphere showed complex wave dynamics, with interference of small-  
 576 scale waves and turbulent regions below what MATS can partly resolve.
- 577 5. Gravity waves had characteristic horizontal wavelengths of 30-40 km for the case study considered in the  
 578 mesopause over Greenland on 25 June 2024.
- 579 6. One peculiar case of the NLC disappearance in the polar mesopause in the afternoon of 24 June 2024 has  
 580 been analyzed. This cloud disappearance was caused by the localized warm spot in the mesopause region  
 581 between Greenland and Scandinavia, as shown by Aura/MLS satellite and JAWARA model data. This warm  
 582 spot in the mesopause region was caused by the intrusion of a warm air mass from middle to high latitudes.
- 583 7. Different movements of NLC were observed in the morning of 25 June 2024 over Greenland. One part of the  
 584 clouds moved to NNE, another one moved to SSW. A detailed analysis of wind data based on the JAWARA

585 model showed that there were different wind systems between 80 and 94 km altitude over Greenland, with a  
586 clockwise wind rotation with altitude. Most likely, a large inertia-gravity wave propagated upwards, causing  
587 significant disturbances (45-50 m/s) of the horizontal wind. The wind disturbances caused NLC to move  
588 differently at different altitudes. Other mechanisms such as the vertical displacement of the NLC layer by  
589 gravity waves may explain the observed different NLC motions.

590 These results demonstrate the scientific value of long-duration stratospheric balloon missions for  
591 mesospheric research. Future campaigns of this type will benefit from expanded multi-spectral imaging, real-  
592 time data transmission, and coordinated ground-satellite observations to further improve understanding of  
593 mesospheric cloud dynamics. A statistical analysis of the wave dynamics observed in NLC during the 2024  
594 TRANSAT balloon flight, and investigation of microphysical properties of NLC ice particles will be addressed  
595 in future studies.

596

#### 597 **Data availability**

598 Two video files of the SONC experiment are available on the Harvard Dataverse repository  
599 (<https://doi.org/10.7910/DVN/AKJK4P>; <https://doi.org/10.7910/DVN/1PHRZU>). Individual NLC images taken  
600 from the stratosphere by the SONC experiment that support the findings of this study are available at the  
601 HEMERA Data Centre (<https://data.hemera-h2020.eu/atmospheric-balloon-experiments/#/>) as well as will be  
602 made available on request.

603

#### 604 **Author contributions**

605 PD, HS, NP, VP, JK and AR have designed two balloon-borne experiments dedicated to studies of noctilucent  
606 clouds and infrasound waves. PD wrote the draft of the paper and made analyses of the SONC images, Esrange  
607 lidar, Aura/MLS and JAWARA data. LM made analysis of the MATS satellite data. PV and JH performed  
608 Esrange lidar measurements. GB performed ALOMAR lidar measurements. DE designed and produced the  
609 electric control unit for the SONC imager. All authors discussed the results and contributed to revisions of the  
610 text and the figures.

611

#### 612 **Competing interests**

613 The contact author has declared that none of the authors has any competing interests.

614

#### 615 **Acknowledgments**

616 The authors thank the CNES/INSU-CNRS Balloon Programme. The TRANSAT balloon flight was funded and  
617 performed by the French Space Agency (CNES) (<https://stratocat.com.ar/fichas-e/2024/KRN-20240622.htm>).  
618 The authors thank the Aura/MLS team for providing temperature and water vapor data around the globe during  
619 the 2024 TRANSAT balloon flight.

620

#### 621 **Financial support**

622 The SONC imager hardware (imager and electronic control unit) was funded by the Kempe Foundation  
623 (Kempestiftelserna) under grant agreement JCK-1901.4. The infrasound instrument and flight costs of the SONC  
624 and infrasound instruments were financed under research grant 42/17 from the Swedish National Space Agency

625 (Rymdstyrelsen). The MATS satellite and JH were financed by the Swedish National Space Agency under grant  
 626 2021-00052. LM was financed by the Swedish National Space Agency under grant 2022-00108 and the Swedish  
 627 Research Council (Vetenskapsrådet) under grant 2021-04876.

628

629 **References**

630 Bailey, S. M., Thomas, G. E., Rusch, D. W., Merkel, A. W., Jeppesen, C., Carstens, J. N., Randall, C. E.,  
 631 McClintock, W. E., and Russell, J. M.: Phase functions of polar mesospheric cloud ice as observed by the CIPS  
 632 instrument on the AIM satellite, *J. Atmos. Sol.-Terr. Phys.*, 71, 3-4, 373–380.

633 <http://dx.doi.org/10.1016/j.jastp.2008.09.039>, 2009.

634 Baumgarten, G., and Fritts, D. C.: Quantifying Kelvin-Helmholtz instability dynamics observed in  
 635 noctilucent clouds: 1. Methods and observations, *J. Geophys. Res. Atmos.*, 119, 9324–9337,  
 636 doi:10.1002/2014JD021832, 2014.

637 Baumgarten, G., Chandran, A., Fiedler, J., Hoffmann, P., Kaifler, N., Lumpe, J., Merkel, A., Randall, C. E.,  
 638 Rusch, D., and Thomas, G.: On the horizontal and temporal structure of noctilucent clouds as observed by  
 639 satellite and lidar at ALOMAR (69N), *Geophys. Res. Lett.*, 39, L01803, doi:10.1029/2011GL049935, 2012.

640 Baumgarten, G.: Doppler Rayleigh/Mie/Raman lidar for wind and temperature measurements in the middle  
 641 atmosphere up to 80 km, *Atmos. Meas. Tech.*, 3, 1509-1518. doi:10.5194/amt-3-1509-2010, 2010.

642 Baumgarten, G., Fiedler, J., Fricke, K. H., Gerding, M., Hervig, M., Hoffmann, P., et al.: The noctilucent  
 643 cloud (NLC) display during the ECOMA/MASS sounding rocket flights on 3 August 2007: morphology on  
 644 global to local scales, *Ann. Geophys.*, 27, 953–965, 2009.

645 Berger, U., and von Zahn, U.: Icy particles in the summer mesopause region: three-dimensional modeling of  
 646 their environment and two-dimensional modeling of their transport, *J. Geophys. Res.*, 107, A11, 1366,  
 647 <https://doi.org/10.1029/2001JA000316>, 2002.

648 Blum, U., and Fricke, K. H.: The Bonn University lidar at the Esrange: technical description and capabilities  
 649 for atmospheric research, *Ann. Geophys.*, 23, 1645–1658, 2005.

650 Chkhetiani, O., and Shalimov, S.: On anomalous wind amplitudes in the lower ionosphere, *J. Atmos. Sol.-*  
 651 *Terr. Phys.*, 240, 105960, <https://doi.org/10.1016/j.jastp.2022.105960>, 2022.

652 Chkhetiani, O. G., and Shalimov, S. L.: Helicity in the upper atmosphere and Ekman-type instabilities, *Dokl.*  
 653 *Earth Sc.*, 431, 345–350, <https://doi.org/10.1134/S1028334X10030177>, 2010.

654 Conte, J. F., Chau, J. L., Renkowitz, T., Latteck, R., Tsutsumi, M., Jacobi, C., Gulbrandsen, N., and Nozawa,  
 655 S.: Observing mesoscale dynamics with multistatic specular meteor radars: first climatology of momentum flux,  
 656 horizontal divergence and relative vorticity over northern central Europe, *Ann. Geophys.*, 43, 603–619,  
 657 <https://doi.org/10.5194/angeo-43-603-2025>, 2025.

658 Dalin, P., Suzuki, H., Pertsev, N., Perminov, V., Efremov, D., Voelger, P., Narayanan, V. L., Mann, I.,  
 659 Häggström, I., Zalcik, M., Ugolnikov, O., Hedin, J., Gumbel, J., Latteck, R., and Baumgarten, G.: Studies of  
 660 noctilucent clouds from the stratosphere during the SONC balloon-borne experiment in 2021. *J. Atmos. Sol.-*  
 661 *Terr. Phys.*, 240, 105959, doi.org/10.1016/j.jastp.2022.105959, 2022.

662 Dalin, P., Pertsev, N., Perminov, V., Efremov, D., and Romejko, V.: Stratospheric observations of  
 663 noctilucent clouds: a new approach in studying middle- and large-scale mesospheric dynamics, *Ann. Geophys.*,  
 664 38, 61–71, <https://doi.org/10.5194/angeo-38-61-2020>, 2020.

- 665 Dalin, P., Pertsev, N., Perminov, V., Efremov, D., and Romejko, V.: Looking at “night-shining” clouds from  
666 the stratosphere, *Eos–AGU*, 100, <https://doi.org/10.1029/2019EO118439>, 2019.
- 667 Dalin, P., Pogoreltsev, A., Pertsev, N., Perminov, V., Shevchuk, N., Dubietis, A., Zalcik, M., et al.: Evidence  
668 of the formation of noctilucent clouds due to propagation of an isolated gravity wave caused by a tropospheric  
669 occluded front, *Geophys. Res. Lett.*, 42, 2037–2046, <https://doi.org/10.1002/2014GL062776>, 2015.
- 670 Dalin, P., Pertsev, N., Dubietis, A., Zalcik, M., Zadorozhny, A., Connors, M., Schofield, I., et al.: A  
671 comparison between ground-based observations of noctilucent clouds and Aura satellite data, *J. Atmos. Sol.-  
672 Terr. Phys.*, 73, 14-15, 2097-2109, <https://doi.org/10.1016/j.jastp.2011.01.020>, 2011.
- 673 Dalin, P., Pertsev, N., Frandsen, S., Hansen, O., Andersen, H., Dubietis, A., and Balciunas, R.: A case study  
674 of the evolution of a Kelvin-Helmholtz wave and turbulence in noctilucent clouds, *J. Atmos. Sol.-Terr. Phys.*,  
675 72, 14-15, 1129-1138, doi:10.1016/j.jastp.2010.06.011, 2010.
- 676 Dalin, P., Pertsev, N., Zadorozhny, A., Connors, M., Schofield, I., Shelton, I., et al.: Ground-based  
677 observations of noctilucent clouds with a northern hemisphere network of automated digital cameras, *J. Atmos.  
678 Sol.-Terr. Phys.*, 70, 1460–1472, 2008.
- 679 DeLand, M. T., and Thomas, G. E.: Updated PMC trends derived from SBUV data, *J. Geophys. Res. Atmos.*,  
680 120, 2140-2166, doi:10.1002/2014JD022253, 2015.
- 681 Demissie, T. D., Espy, P. J., Kleinknecht, N. H., Hatlen, M., Kaifler, N., and Baumgarten, G.: Characteristics  
682 and sources of gravity waves observed in noctilucent cloud over Norway, *Atmos. Chem. Phys.*, 14, 12133–  
683 12142, doi:10.5194/acp-14-12133-2014, 2014.
- 684 Dubinskii, A. Yu., and Popel, S. I.: Formation and evolution of dusty plasma structures in the ionosphere,  
685 *JETP Lett.*, 96, 21–26, doi:10.1134/S0021364012130048, 2012.
- 686 Eckermann, S. D.: Hodographic analysis of gravity waves: relationships among Stokes parameters, rotary  
687 spectra and cross-spectral methods, *J. Geophys. Res.*, 101, 19169–19174, 1996.
- 688 Fiedler, J., Baumgarten, G., Berger, U., Hoffmann, P., Kaifler, N., and Lübken, F.-J.: NLC and the  
689 background atmosphere above ALOMAR, *Atmos. Chem. Phys.*, 11, 5701–5717. doi:10.5194/acp-11-5701-2011,  
690 2011.
- 691 Fritts, D. C., Wang, L., Baumgarten, G., Miller, A. D., Geller, M. A., Jones, G., Limon, M., Chapman, D.,  
692 Didier, J., et al.: High-resolution observations and modeling of turbulence sources, structures, and intensities in  
693 the upper mesosphere, *J. Atmos. Sol.-Terr. Phys.*, 162, 57-78, <https://doi.org/10.1016/j.jastp.2016.11.006>, 2017.
- 694 Fritts, D. C., Miller, A. D., Kjellstrand, C. B., Geach, C., Williams, B. P., Kaifler, B., et al.: PMC Turbo:  
695 Studying gravity wave and instability dynamics in the summer mesosphere using polar mesospheric cloud  
696 imaging and profiling from a stratospheric balloon, *J. Geophys. Res. Atmos.*, 124, 6423–6443.  
697 <https://doi.org/10.1029/2019JD030298>, 2019.
- 698 Froidevaux, L., Livesey, N. J., Read, W. G., Jiang, Y. B., Jiménez, C. C., Filipiak, M. J., Schwartz, M. J., et  
699 al.: Early validation analyses of atmospheric profiles from EOS MLS on the Aura satellite, *IEEE Transactions on  
700 Geoscience and Remote Sensing*, 44, 5, 1106-1121, 2006.
- 701 Gadsden, M., and Schröder, W.: *Noctilucent Clouds*, Springer, New York, 1989.
- 702 Gao, H., Shepherd, G. G., Tang, Y., Bu, L., and Wang, Z.: Double-layer structure in polar mesospheric  
703 clouds observed from SOFIE/AIM, *Ann. Geophys.*, 35, 295–309, <https://doi.org/10.5194/angeo-35-295-2017>,  
704 2017.

- 705 Gerding, M., Höffner, J., Hoffmann, P., Kopp, M., and Lübken, F.-J.: Noctilucent cloud variability and mean  
706 parameters from 15 years of lidar observations at a mid-latitude site (54°N, 12°E), *J. Geophys. Res. Atmos.*, 118,  
707 317–328, <https://doi.org/10.1029/2012JD018319>, 2013.
- 708 Gossard, E. E., and Hooke, W. H.: *Waves in the atmosphere: atmospheric infrasound and gravity waves –*  
709 *their generation and propagation*, Elsevier Scientific Publishing Co, Amsterdam, 1975.
- 710 Gumbel, J., Megner, L., Christensen, O. M., Ivchenko, N., Murtagh, D. P., Chang, S., Dillner, J., Ekebrand, T.,  
711 Giono, G., Hammar, A., Hedin, J., et al.: The MATS satellite mission – gravity wave studies by Mesospheric  
712 Airglow/Aerosol Tomography and Spectroscopy, *Atmos. Chem. Phys.*, 20, 431–455, [https://doi.org/10.5194/acp-](https://doi.org/10.5194/acp-20-431-2020)  
713 [20-431-2020](https://doi.org/10.5194/acp-20-431-2020), 2020.
- 714 Gumbel, J., and Witt, G.: Rocket-borne photometry of NLC particle populations, *Adv. Space Res.*, 28, 7, 1053-  
715 1058, 2001.
- 716 Hervig, M. E., Siskind, D. E., Bailey, S. M., and Russell III, J. M.: The influence of PMCs on water vapor and  
717 drivers behind PMC variability from SOFIE observations, *J. Atmos. Sol.-Terr. Phys.*, 132, 124-134,  
718 <https://doi.org/10.1016/j.jastp.2015.07.010>, 2015.
- 719 Kaifler, N., Baumgarten, G., Klekociuk, A. R., Alexander, S. P., Fiedler, J., and Lübken, F.-J.: Small scale  
720 structures of NLC observed by lidar at 69°N/69°S and their possible relation to gravity waves, *J. Atmos. Sol.-*  
721 *Terr. Phys.*, 104, 244–252, doi:10.1016/j.jastp.2013.01.004, 2013.
- 722 Karlsson, B., and Gumbel, J.: Challenges in the limb retrieval of noctilucent cloud properties from  
723 Odin/OSIRIS, *Adv. Space Res.*, 36, 935-942, doi:10.1016/j.asr.2005.04.074, 2005.
- 724 Koshin, D., Sato, K., Miyazaki, K., and Watanabe, S.: An ensemble Kalman filter data assimilation system  
725 for the whole neutral atmosphere, *Geosci. Model Dev.*, 13, 3145–3177, [https://doi.org/10.5194/gmd-13-3145-](https://doi.org/10.5194/gmd-13-3145-2020)  
726 [2020](https://doi.org/10.5194/gmd-13-3145-2020), 2020.
- 727 Koshin, D., Sato, K., Kohma, M., and Watanabe, S.: An update on the 4D-LETKF data assimilation system  
728 for the whole neutral atmosphere, *Geosci. Model Dev.*, 15, 2293–2307, [https://doi.org/10.5194/gmd-15-2293-](https://doi.org/10.5194/gmd-15-2293-2022)  
729 [2022](https://doi.org/10.5194/gmd-15-2293-2022), 2022.
- 730 Koshin, D., Sato, K., Watanabe, S., et al.: The JAGUAR-DAS whole neutral atmosphere reanalysis:  
731 JAWARA, *Prog. Earth Planet. Sci.*, 12, 1, <https://doi.org/10.1186/s40645-024-00674-3>, 2025.
- 732 Lambert, A., Read, W. G., Livesey, N. J., Santee, M. L., Manney, G. L., Froidevaux, L., Wu, D. L.,  
733 Schwartz, M. J., Pumphrey, H. C., Jimenez, C., Nedoluha, G. E., et al.: Validation of the Aura Microwave Limb  
734 Sounder middle atmosphere water vapor and nitrous oxide measurements, *J. Geophys. Res.*, 112, D24S36, 2007.
- 735 Li, H., Wu, J., and Zhou, Z.: The formation of multiple layers of ice particles in the polar summer mesopause  
736 region, *Ann. Geophys.*, 34, 117–122, doi:10.5194/angeo-34-117-2016, 2016.
- 737 Liu, X., Yue, J., Xu, J., Yuan, W., Russell III, J. M., Hervig, M. E., and Nakamura, T.: Persistent longitudinal  
738 variations in 8 years of CIPS/AIM polar mesospheric clouds, *J. Geophys. Res. Atmos.*, 121, 8390–8409,  
739 doi:10.1002/2015JD024624, 2016.
- 740 Megner, L., Gumbel, J., Christensen, O. M., Linder, B., Murtagh, D., Ivchenko, N., Krasauskas, L., Hedin, J.,  
741 Dillner, J., and Stegman, J.: MATS satellite images (level 1b) of airglow and noctilucent clouds in the  
742 mesosphere/lower thermosphere, February–May 2023, Dataset version 1.0, Bolin Centre Database,  
743 <https://doi.org/10.17043/mats-level-1b-limb-cropd-1.0>, 2025.

- 744 Miller, A. D., Fritts, D. C., Chapman, D., Jones, G., Limon, M., Araujo, D., et al.: Stratospheric imaging of  
 745 polar mesospheric clouds: a new window on small-scale atmospheric dynamics, *Geophys. Res. Lett.*, 42, 6058–  
 746 6065, doi:10.1002/2015GL064758, 2015.
- 747 Murphy, D. M., and Koop, T.: Review of the vapour pressures of ice and supercooled water for atmospheric  
 748 applications, *Q. J. R. Meteorol. Soc.*, 131, 1539–1565. doi:10.1256/qj.04.94, 2005.
- 749 Pautet, P.-D., Stegman, J., Wrasse, C. M., Nielsen, K., Takahashi, H., Taylor, M. J., et al.: Analysis of gravity  
 750 waves structures visible in noctilucent cloud images, *J. Atmos. Sol.-Terr. Phys.*, 73, 14-15, 2082-2090, doi:  
 751 10.1016/j.jastp.2010.06.001, 2011.
- 752 Pertsev, N. N., Dalin, P. A., Perminov, V. I., Gusev, N. K., Tsimerinov, E. Yu., Solodovnik, A. A.,  
 753 Zadorozhny, A. M., Korotyshkin, D. V., and Bordonskiy, G. S.: Analysis of noctilucent cloud fields according to  
 754 ground-based network and airborne photography data, *Izv. Atmos. Ocean. Phys.*, 60, 2, 187–194,  
 755 doi.org/10.1134/S0001433824700191, 2024.
- 756 Portnyagin, Y. I. and Solovjova, T. V.: Global empirical wind model for the upper mesosphere/lower  
 757 thermosphere. I. Prevailing wind, *Ann. Geophys.*, 18, 300–315, <https://doi.org/10.1007/s00585-000-0300-y>,  
 758 2000.
- 759 Randall, C. E., Carstens, J., France, J. A., Harvey, V. L., Hoffmann, L., Bailey, S. M., Alexander, M.  
 760 J., Lumpe, J. D., Yue, J. et al.: New AIM/CIPS global observations of gravity waves near 50–55 km, *Geophys.*  
 761 *Res. Lett.*, 44, 7044–7052, <https://doi.org/10.1002/2017GL073943>, 2017.
- 762 Rapp, M., Lubken, F.-J., Müllemann, A., Thomas, G. E., and Jensen, E. J.: Small-scale temperature  
 763 variations in the vicinity of NLC: Experimental and model results, *J. Geophys. Res.*, 107, D19, 4392,  
 764 doi:10.1029/2001JD001241, 2002.
- 765 Read, W. G., Lambert, A., Bacmeister, J., Cofield, R. E., Christensen, L. E., Cuddy, D. T., Daffer, W. H.,  
 766 Drouin, B. J., Fetzer, E., Froidevaux, et al.: Aura Microwave Limb Sounder upper tropospheric and lower  
 767 stratospheric H<sub>2</sub>O and relative humidity with respect to ice validation, *J. Geophys. Res.*, 112, D24S35, 2007.
- 768 Reimuller, J. D., Thayer, J. P., Baumgarten, G., Chandran, A., Hulley, B., Rusch, D., Nielsen, K., and  
 769 Lumpe, J.: Synchronized imagery of noctilucent clouds at the day-night terminator using airborne and  
 770 spaceborne platforms, *J. Atmos. Sol.-Terr. Phys.*, 73, 14-15, 2091-2096, 2011.
- 771 Schwartz, M. J., Lambert, A., Manney, G. L., Read, W. G., Livesey, N. J., Froidevaux, L., Ao, C. O.,  
 772 Bernath, P. F., Boone, C. D., Cofield, R. E., et al.: Validation of the Aura Microwave Limb Sounder temperature  
 773 and geopotential height measurements, *J. Geophys. Res.*, 113, D15S11, 2008.
- 774 Suzuki, H., Matsumoto, A., Dalin, P., Nakamura, Y., Ishii, S., Sakanoi, K., Sakaguchi, K., Takada, T., Tsuda,  
 775 T. T., and Hozumi, Y.: Capability of airline jets as an observation platform for noctilucent clouds at middle  
 776 latitudes, *Prog. Earth Planet. Sci.*, 9, 11, <https://doi.org/10.1186/s40645-022-00469-4>, 2022.
- 777 Thomas, G.E.: Solar Mesosphere Explorer measurements of polar mesospheric clouds (noctilucent clouds), *J.*  
 778 *Atmos. Terr. Phys.*, 46, 9, 819-824, 1984.
- 779 Tsuda, T. T., Hozumi, Y., Kawaura, K., Tatsuzawa, K., Ando, Y., Hosokawa, K., et al.: Detection of polar  
 780 mesospheric clouds utilizing Himawari-8/AHI full-disk images, *Earth Space Sci.*, 9,  
 781 2021EA002076, <https://doi.org/10.1029/2021EA002076>, 2022.
- 782 Wallis, S., DeLand, M., and Savigny, C.: Did the 2022 Hunga eruption impact the noctilucent cloud season in  
 783 2023/24 and 2024?, *Atmos. Chem. Phys.*, 25, 3635–3645. <https://doi.org/10.5194/acp-25-3635-2025>, 2025.

784 Zadorozhny, A. M., Tyutin, A. A., Witt, G., Wilhelm, N., Wälchli, U., Cho, J. Y. N., and Swartz, W. E.:  
785 Electric field measurements in the vicinity of noctilucent clouds and PMSE, *Geophys. Res. Lett.*, 20, 20, 2299-  
786 2302, 1993.